Supporting Information (SI)

Ultrafast spectroscopy of Ru^{II} polypyridine complexes in gas phase and liquid phase: $[Ru(2,2'\text{-bipyridine})_2(nicotinamide)_2]^{2+}$

L. Schüssler,[†a] R. G. E. Israil, [†b] P. Hütchen,[c] W. R. Thiel,[c] R. Diller,[*a] C. Riehn*[b,d]

[a.] Department of Physics, Technische Universität Kaiserslautern (TUK)
Erwin-Schrödinger-Str. 46, D-67663 Kaiserslautern, Germany
E-Mail: diller@physik.uni-kl.de; Tel: +49 631 2052323

[b.] Department of Chemistry, Technische Universität Kaiserslautern (TUK)
Erwin-Schrödinger-Str. 52, D-67663 Kaiserslautern, Germany
E-Mail: riehn@chemie.uni-kl.de; Tel: +49 631 2054859

[c.] Department of Chemistry, Technische Universität Kaiserslautern (TUK)
Erwin-Schrödinger-Str. 54, D-67663 Kaiserslautern, Germany

[d.] Research Center OPTIMAS
Erwin-Schrödinger Str.46, D-67663 Kaiserslautern, Germany

[†] Contributed equally to this work.

Table of Contents

1. Additional Information on Experimental Methods

Femtosecond transient absorption spectroscopy

The irradiation of $[Ru(bpy)_2(na)_2]^{2+}$ (**1**) leads to the formation of the mono-aquated photoproduct $[Ru(bpy)_2(na)(H_2O)]^{2+}$ (**2**).[1] Thus, in the rotating cell a slow irreversible depletion of **1** and a concomitant (slow) formation and accumulation of the monoaqua species **2** occurred during the measurements. In consequence, the observed photoinduced fs-dynamics changed along the ongoing measurement according to the decreasing ratio of **1** and **2**. After five or ten measurement cycles the dynamics obviously shifted from the dynamics dominated by **1** in the early cycles to the dynamics dominated by **2** (see dashed line in SI-Fig. 1a).

In order to distinguish and to capture the respective (changing) contributions of **1** and **2** during the measurements the data of the various measurement cycles were not averaged but analyzed separately. By thorough comparison of the changes over the cycles, an assignment of the total five found time constants to either **1** or to **2** was possible (e.g. via the development, i.e. de- and increase of the amplitudes, of the corresponding DAS). It turns out that the first cycle represents the dynamics of **1** without a significant contribution of **2** and only the four time constants (Tab. 3) for **1** were found. Thus, only the results of the first cycle are presented for **1** in the rotating cell. In the subsequent cycles, only minor changes for τ_1 - τ_3 were found, due to the similarities of these components for both **1** and **2**. But while the amplitude of the DAS of the 83 ps component of **2** increases over the cycles, the amplitude of the ~ 180 ps component of **1** decreases. This procedure and corresponding results were justified and confirmed by the following two experiments (i) and (ii). (i) The fs absorption measurement on exclusively **2** in the rotating cell revealed results fully consistent with those of the former analysis (i.e. the experiment on **1** with accumulated **2)**. (ii) The fs measurement on **1** excited at 340 nm in the flow cell (without significant photoproduct accumulation) again led to the same results as the measurement in the rotating cell. The results of the flow cell measurement are presented in Fig. 6 and the corresponding rotating cell measurement results are shown in SI-Fig. 1.

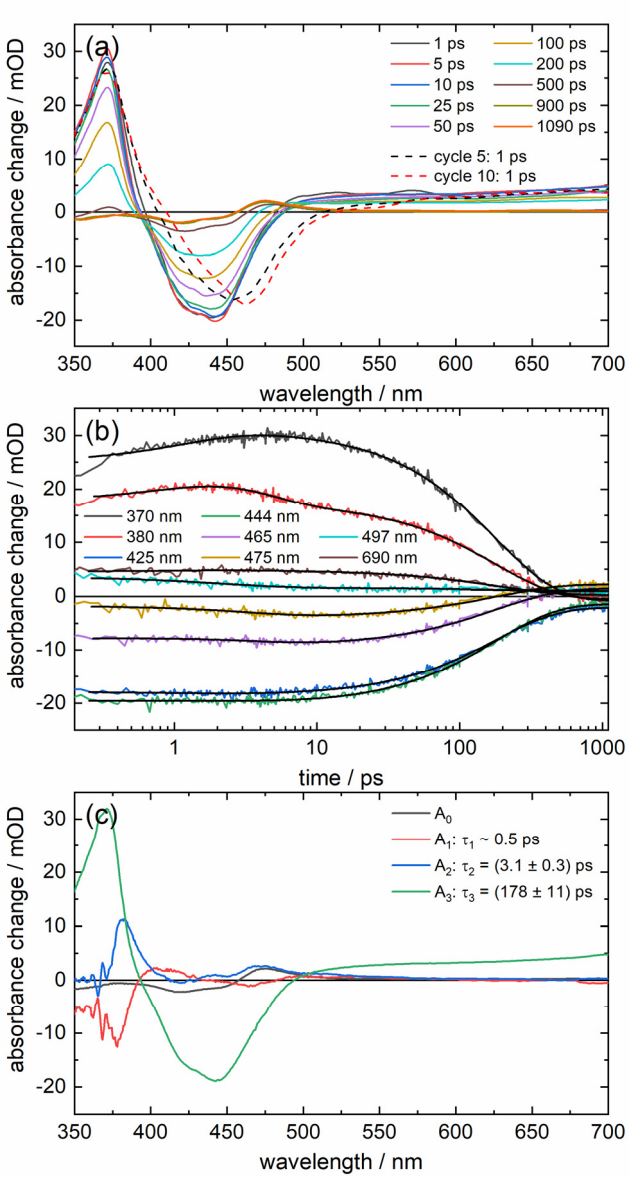

Figure 1 Difference spectra at selected delay times (a), absorbance transients at selected wavelengths (b) and decay associated spectra (DAS) (c) for $[Ru(bpy)_2(na)_2]^{2+}$ (**1**) in H_2O excited at 340 nm (rotating cell). Dashed lines in (a): Difference spectra at 1 ps delay time of the fifth and tenth measurement cycle, respectively. Solid black line in (b): Result of a global analysis according to eq. (2) in main text.

2. Mass Spectra and CID Curves

The compound $[Ru(bpy)_2(na)_2](PF_6)_2$ (**1**$(PF_6)_2$) is dissolvable in acetonitrile (ACN), methanol, and tetrahydrofuran, whereas in acetone slightly soluable and in dichloromethane a very low solubility was observed. We have chosen ACN for all ion trap investigations since it complies best with ESI. Additionally, we have tested the immediate and long-term solvolysis of **1** in several other solvents (SI-Fig. 2).

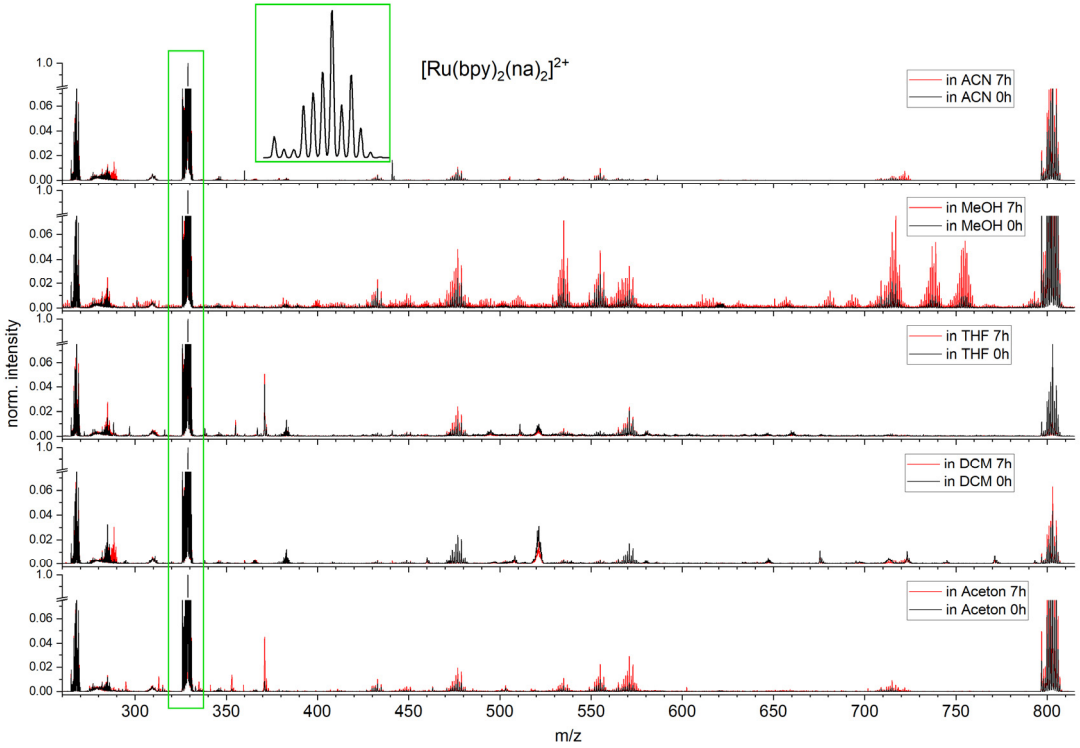

Figure 2 Mass spectra of $[Ru(bpy)_2(na)_2]^{2+}$ $2(PF_6)^-$ (**1**$(PF_6)_2$) of a freshly prepared solution (black) and after 7 h (red), interrupted scale from 0.075 to 0.9; main peak at 329 m/z (mark).

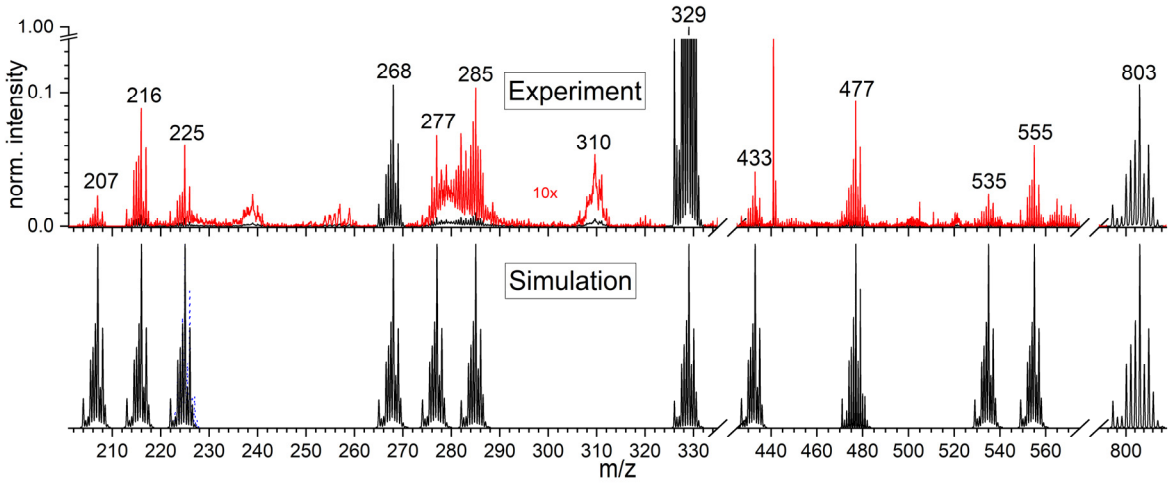

Figure 3 ESI Mass spectrum of $[Ru(bpy)_2(na)_2](PF_6)_2$ (**1**$(PF_6)_2$) from ACN solution and simulations of the isotope patterns of the observed species.

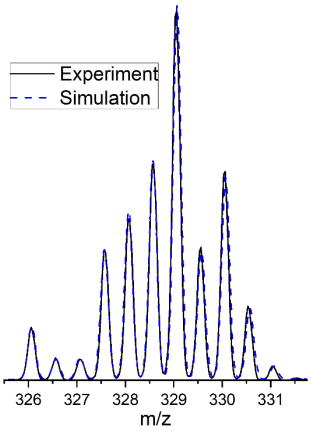

Figure 4 ESI Mass spectrometric pattern of $[Ru(bpy)_2(na)_2]^{2+}$ (**1**) and its simulation at m/z 329.

Table 1 Assignment of fragments to the measured overview mass spectrum of $[Ru(bpy)_2(na)_2]^{2+}$ (**1**). The main peak at 329 m/z (bold).

monoisotopic m/z	assignment	composition
(207)	$[Ru^{II}(bpy)_2]^{2+}$	$Ru(C_{10}H_8N_2)_2$
216	$[Ru^{II}(bpy)_2(H_2O)]^{2+}$	$Ru(C_{10}H_8N_2)_2(H_2O)$
225	$[Ru^{II}(bpy)_2(H_2O)_2]^{2+}$ or $[Ru^{II}(bpy)_2(HCl)]^{2+}$	$Ru(C_{10}H_8N_2)_2(H_2O)_2$ or $Ru(C_{10}H_8N_2)_2(HCl)$
268	$[Ru^{II}(bpy)_2(NA)_1]^{2+}$ (PCI)	$Ru(C_{10}H_8N_2)_2(C_6H_6N_2O)_1$
277	$[Ru^{II}(bpy)_2(NA)_1\ (H_2O)]^{2+}$	$Ru(C_{10}H_8N_2)_2(C_6H_6N_2O)_1\ (H_2O)$
285	$[Ru^{II}(bpy)_3]^{2+}$	$Ru(C_{10}H_8N_2)_3$
329	**$[Ru^{II}(bpy)_2(na)_2]^{2+}$**	**$Ru(C_{10}H_8N_2)_2(C_6H_6N_2O)_2$**
433	$[Ru^{II}(bpy)_2F]^{+}$	$Ru(C_{10}H_8N_2)_2F$
477	$[Ru^{II}(bpy)_2(Cl)(CO)]^{+}$	$Ru(C_{10}H_8N_2)_2(Cl)(CO)$
535	$[Ru^{II}(bpy)_2(NA)_1]^{+}$ -H	$Ru(C_{10}H_8N_2)_2(C_6H_5N_2O)_1$
555	$[Ru^{II}(bpy)_2(NA)_1F]^{+}$	$Ru(C_{10}H_8N_2)_2(C_6H_6N_2O)_1F$
803	$[Ru^{II}(bpy)_2(NA)_2(PF_6)]^{+}$	$Ru(C_{10}H_8N_2)_2(C_6H_6N_2O)_2(PF_6)$

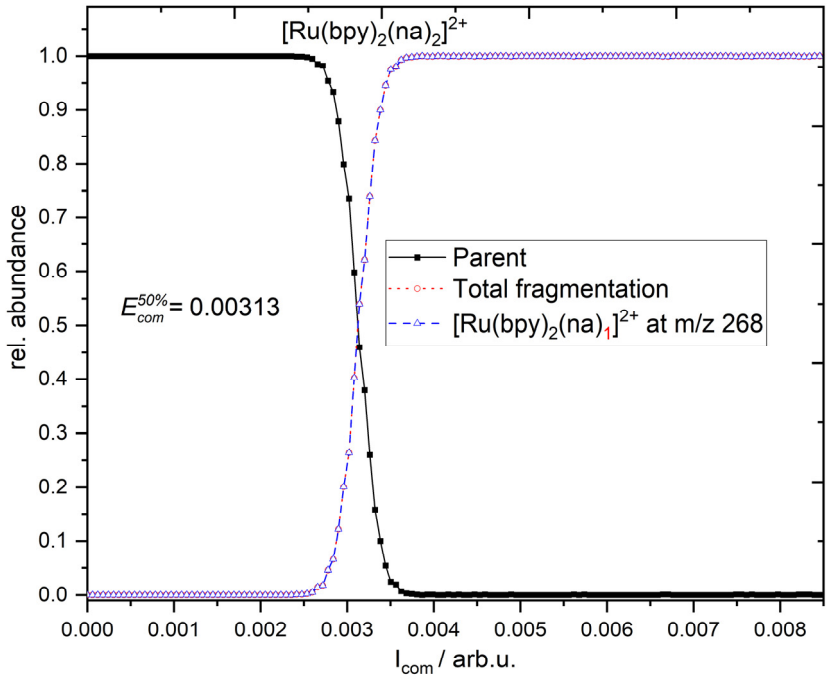

Figure 5 CID curve of $[Ru(bpy)_2(na)_2]^{2+}$ (**1**). $\mathbf{E_{com}^{50\%}}$ value determined through sigmoidal fitting of the total fragmentation curve.

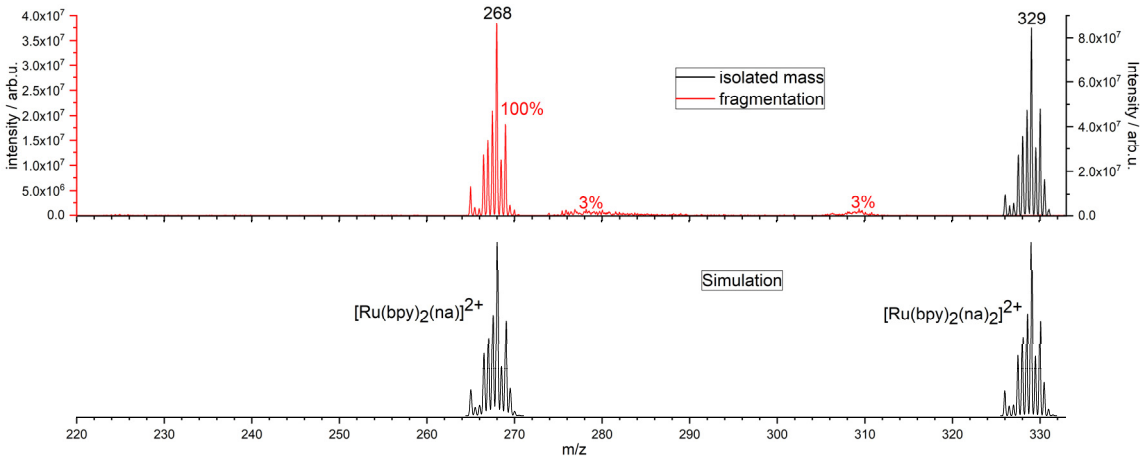

Figure 6 Mass spectrum of the isolated main species $[Ru(bpy)_2(na)_2]^{2+}$ (**1**), its fragmentation via CID and its relative intensity (red); simulations shown below.

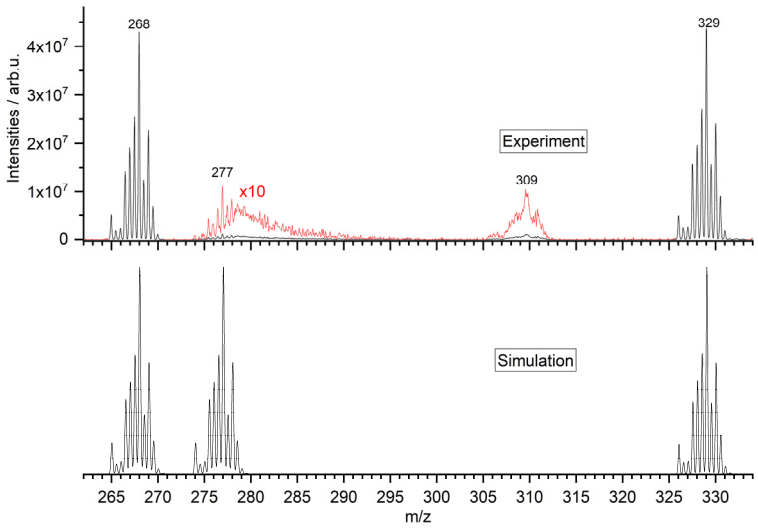

Figure 7 Mass spectrum of the isolated main species $[Ru(bpy)_2(na)_2]^{2+}$ (**1**) after photodissociation (270 nm, 2 µJ) and simulations of the isotope patterns of the observed species. Red trace presents magnification by 10x.

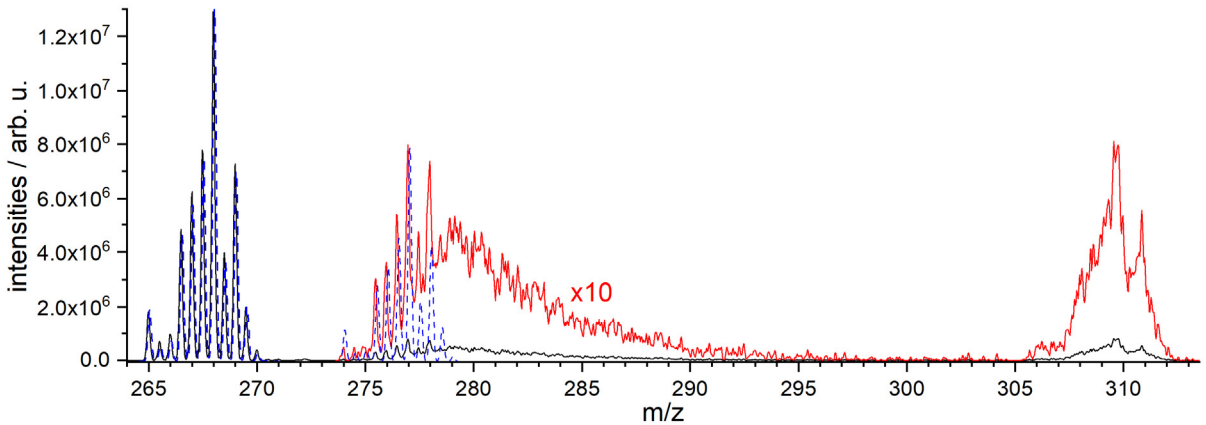

Figure 8 Mass spectrum of the isolated species $[Ru(bpy)_2(na)]^{2+}$ (PCI) at m/z 268 (black). Red presents the magnified intensity by 10 and blue the simulation of PCI and PCI-H_2O.

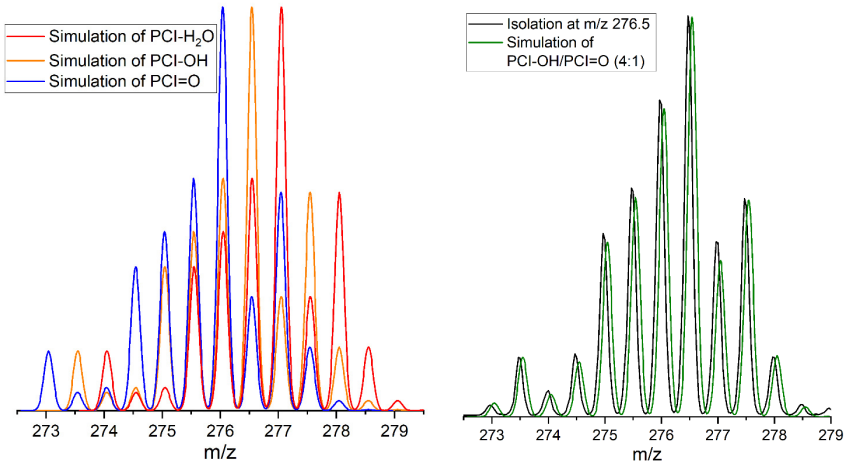

Figure 9 Left: simulated isotope pattern of PCI-H_2O, PCI-OH and PCI-O. Right: mass spectrum after isolation of m/z 276.5 (black), and its simulation of PCI-OH/PCI-O in a 4:1 ratio (green). See also the electrochemical generation of similar species.[2, 3]

Table 2 Composition and nominal masses of penta-coordinated intermediate (PCI) and related species of different Ru oxidation states (PCI-H_2O, PCI-OH, PCI-O).

Dissolving	nominal m/z	assignment	Abbreviation
$[Ru(bpy)_2(na)_2](PF_6)_2$ in ACN	268	$[Ru^{II}(bpy)_2(na)_1]^{2+}$	PCI
	277	$[Ru^{II}(bpy)_2(na)_1(H_2O)]^{2+}$	PCI-H_2O
$[Ru(bpy)_2(na)_2](PF_6)_2$ in H_2O	276.5	$[Ru^{III}(bpy)_2(na)_1(OH)]^{2+}$	PCI-OH
	276	$[Ru^{IV}(bpy)_2(na)_1(O)]^{2+}$	PCI-O

3. UV-PD Spectra, Calculated Absorption Spectra, Comparison with Solution Absorption Spectra

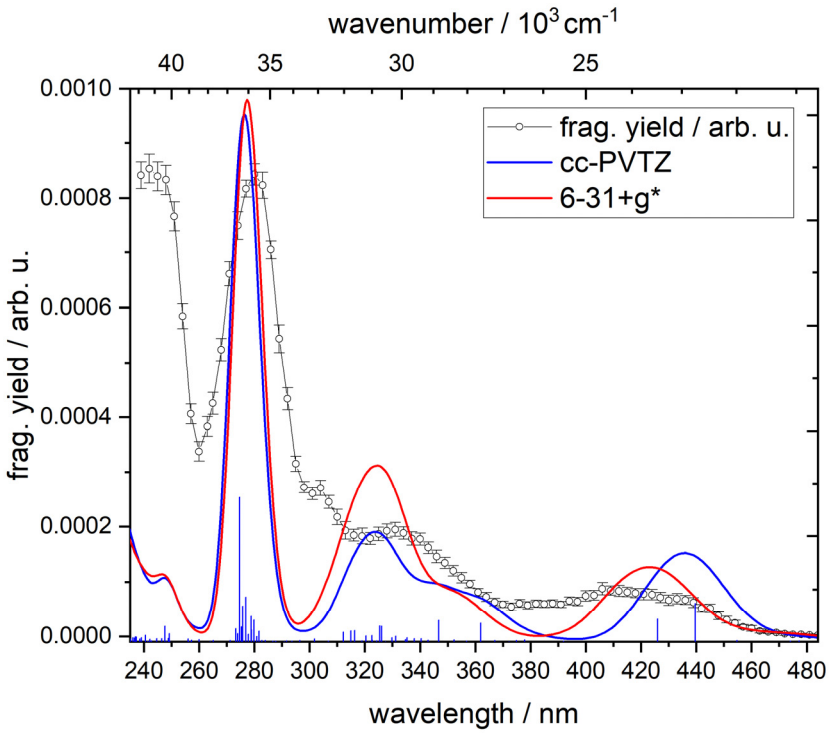

Figure 10 Gas phase UV PD spectrum (grey) of $[Ru(bpy)_2(na)_2]^{2+}$ (**1**) and calculated spectra obtained at the TD-DFT/B3LYP/6-31+G* (red) and cc-PVTZ (blue) level of theory (convoluted with 3000 cm^{-1} FWHM Gaussian).

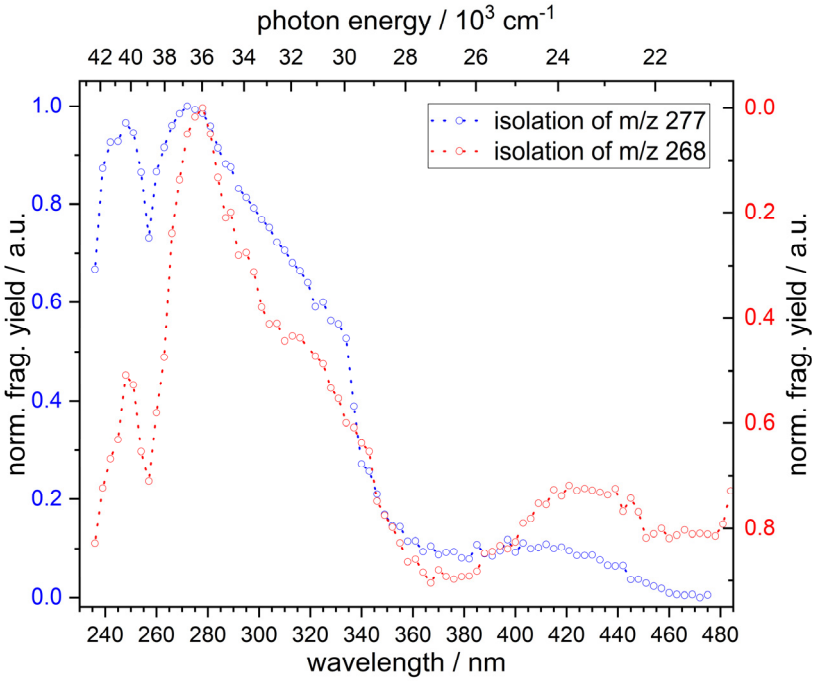

Figure 11 Gas phase UV PD spectra resulting from irradiation of the isolation at m/z 268 (PCI, red) and m/z 277 (PCI-H_2O, blue).

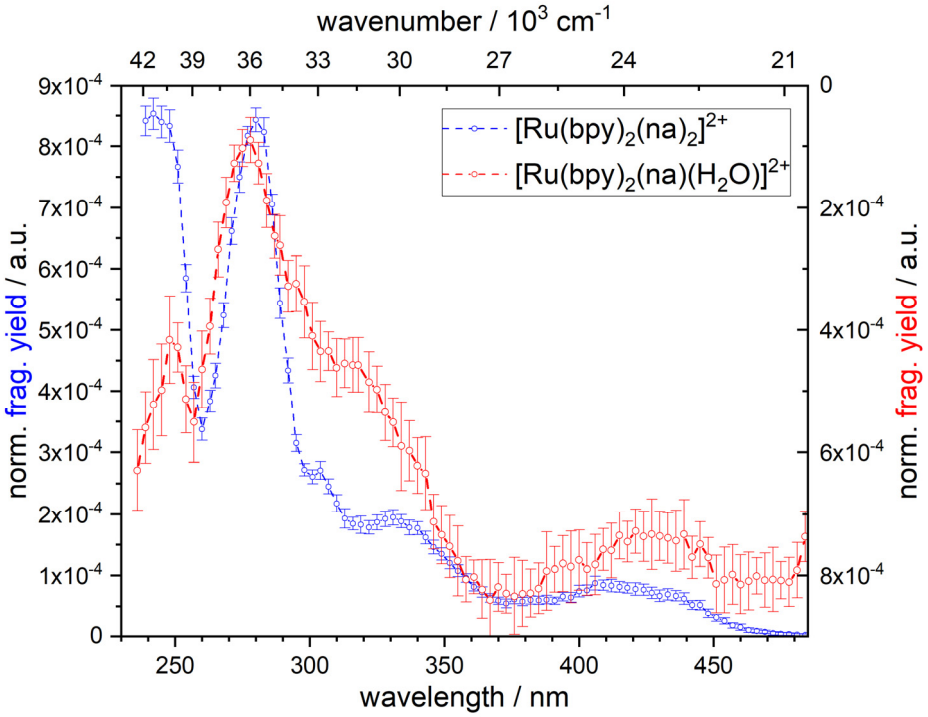

Figure 12 Gas phase UV PD spectrum (blue) of $[Ru(bpy)_2(na)_2]^{2+}$ (**1**) and of $[Ru(bpy)_2(na)(H_2O)]^{2+}$ (**2**, PCI-H_2O) (red).

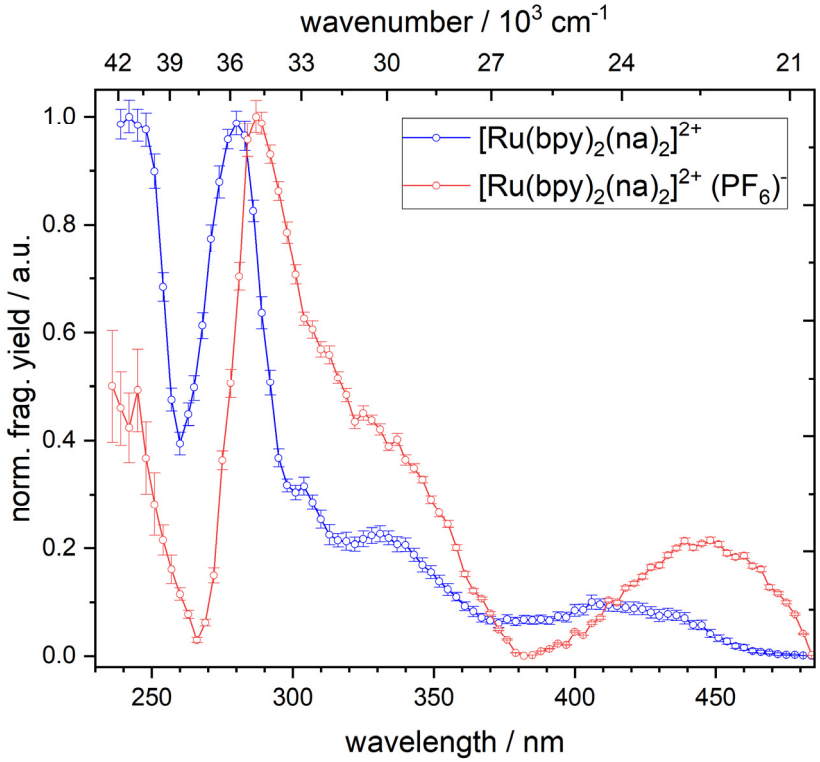

Figure 13 Gas phase UV PD spectrum (blue) of $[Ru(bpy)_2(na)_2]^{2+}$ (**1**) and of $[Ru(bpy)_2(na)_2]^{2+}(PF_6)^-$ (red).

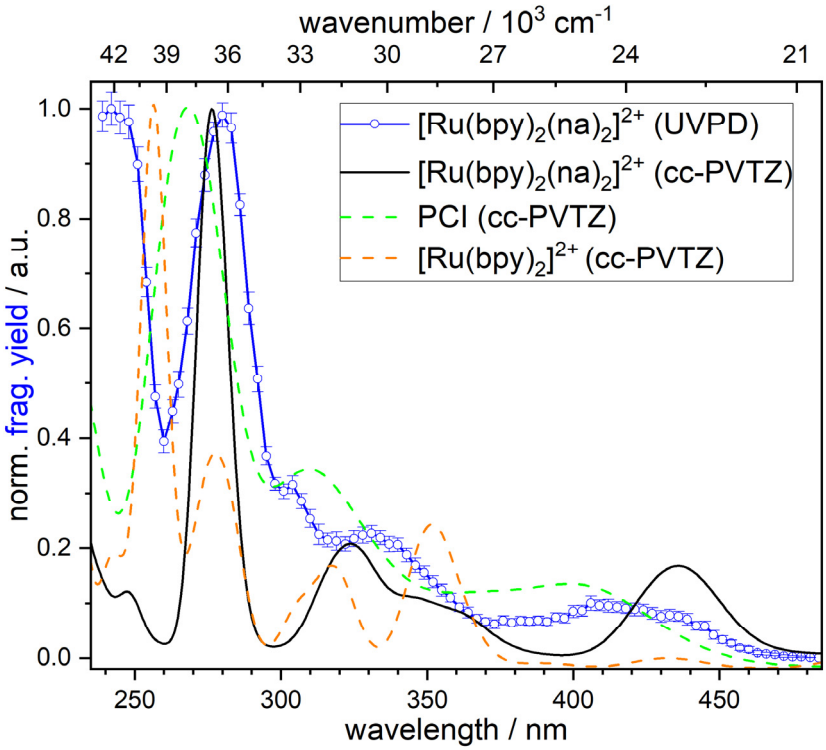

Figure 14 Gas phase UV PD spectrum of $[Ru(bpy)_2(na)_2]^{2+}$ (**1**) (blue) and calculated absorption spectra of $[Ru(bpy)_2(na)_2]^{2+}$ (**1**) (black), $[Ru(bpy)_2(na)]^{2+}$ (PCI, green) and $[Ru(bpy)_2]^{2+}$ (orange) obtained at the TD-DFT/B3LYP/cc-PVTZ level of theory (convoluted with 1500 cm^{-1} FWHM Gaussians).

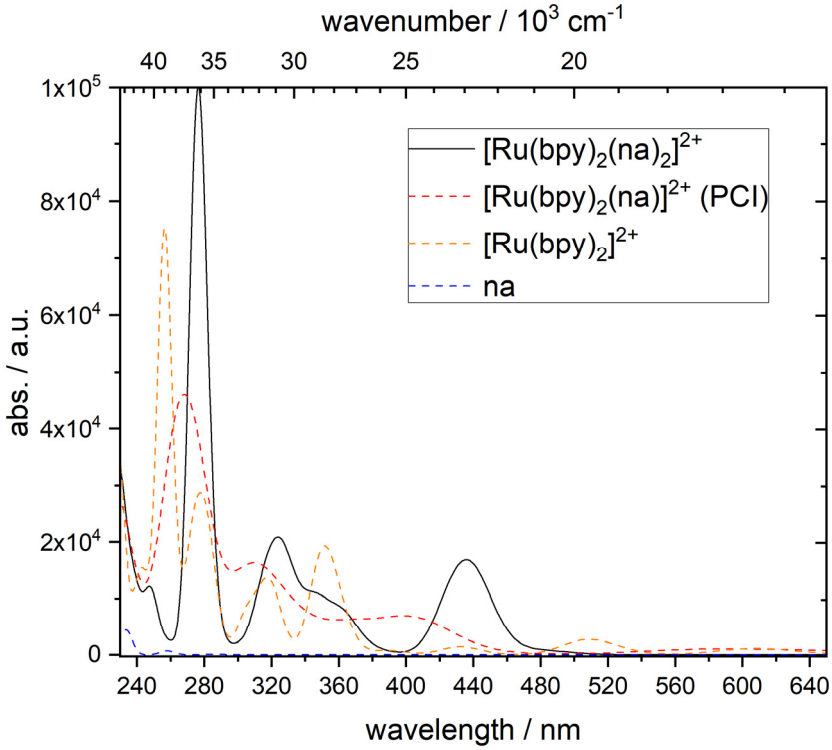

Figure 15 Calculated absorption spectra of $[Ru(bpy)_2(na)_2]^{2+}$ (**1**), $[Ru(bpy)_2(na)]^{2+}$ (PCI), $[Ru(bpy)_2]^{2+}$, and the nicotinamid ligand (na) obtained at the TD-DFT/B3LYP/cc-PVTZ level of theory (convoluted with 1500 cm^{-1} FWHM Gaussians).

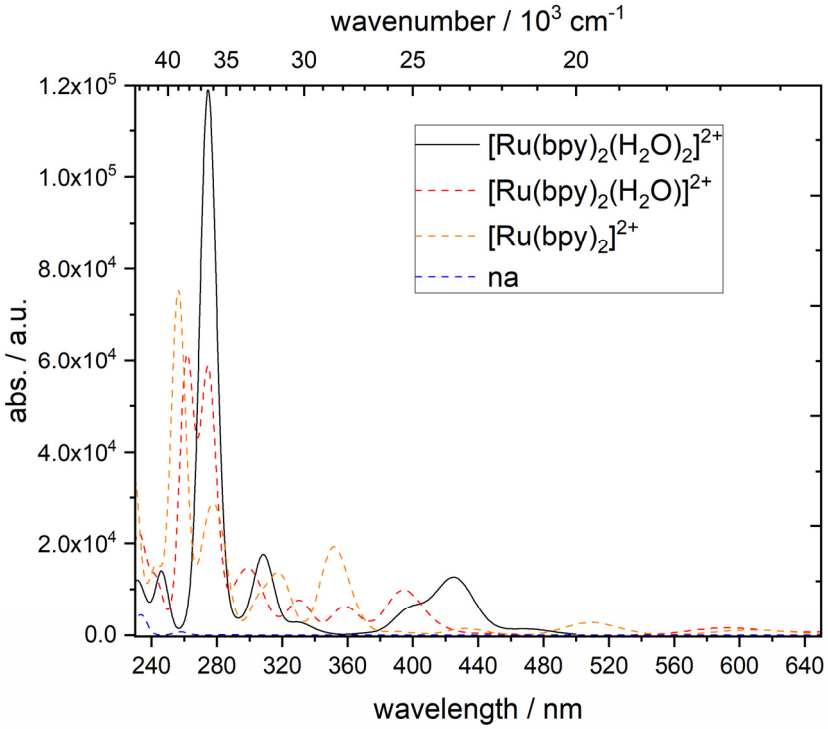

Figure 16 Calculated absorption spectra of $[Ru(bpy)_2(H_2O)_2]^{2+}$, $[Ru(bpy)_2(H_2O)]^{2+}$, $[Ru(bpy)_2]^{2+}$, and the nicotinamid ligand (na) obtained at the TD-DFT/B3LYP/cc-PVTZ level of theory (convoluted with 1500 cm^{-1} FWHM Gaussians).

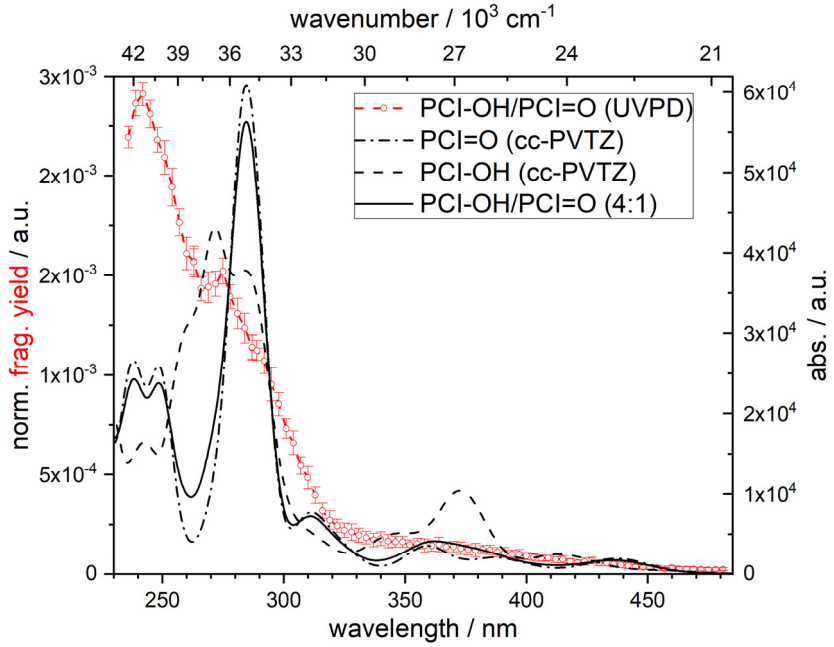

Figure 17 Gas phase UV PD spectrum (red) of $[Ru(bpy)_2(na)(OH)]^{2+}$/$[Ru(bpy)_2(na)(O)]^{2+}$ (PCI-OH/PCI-O) and the calculated spectra (dotted) of $[Ru(bpy)_2(na)(OH)]^{2+}$ (PCI-OH) and $[Ru(bpy)_2(na)(O)]^{2+}$ (PCI-O) obtained at the TD-DFT/B3LYP/cc-PVTZ level of theory (convoluted with 1500 cm^{-1} FWHM Gaussians). The black-lined curve represents the calculated spectra of PCI-OH/PCI-O in an 4:1 ratio.

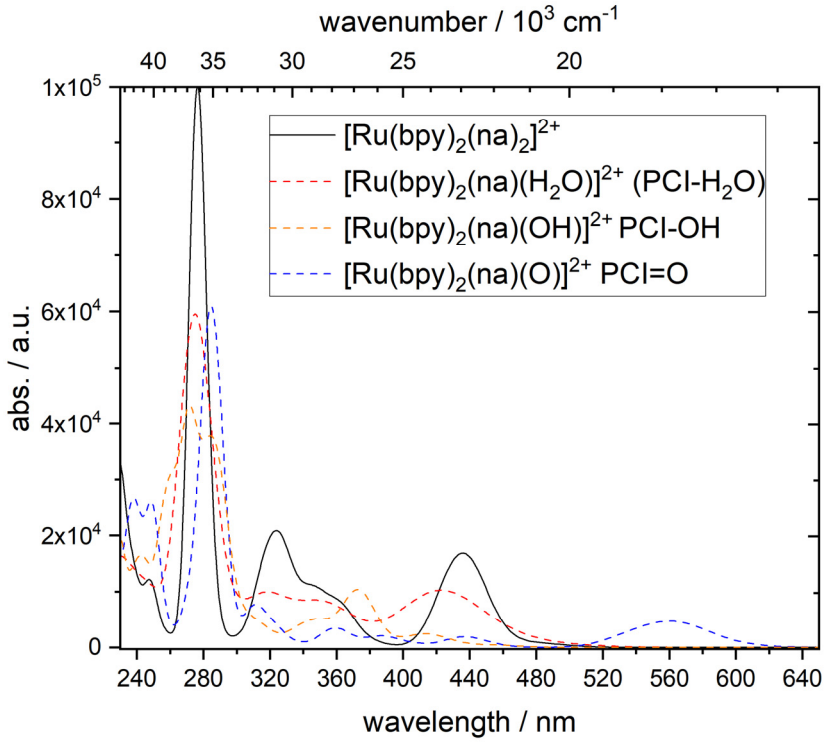

Figure 18 Calculated absorption spectra of $[Ru(bpy)_2(na)_2]^{2+}$ (**1**), PCI-H_2O ($[Ru(bpy)_2(na)(H_2O)]^{2+}$), PCI-OH ($[Ru(bpy)_2(na)(OH)]^{2+}$) and PCI=O ($[Ru(bpy)_2(na)(O)]^{2+}$) obtained at the TD-DFT/B3LYP/cc-PVTZ level of theory (convoluted with 1500 cm^{-1} FWHM Gaussians).

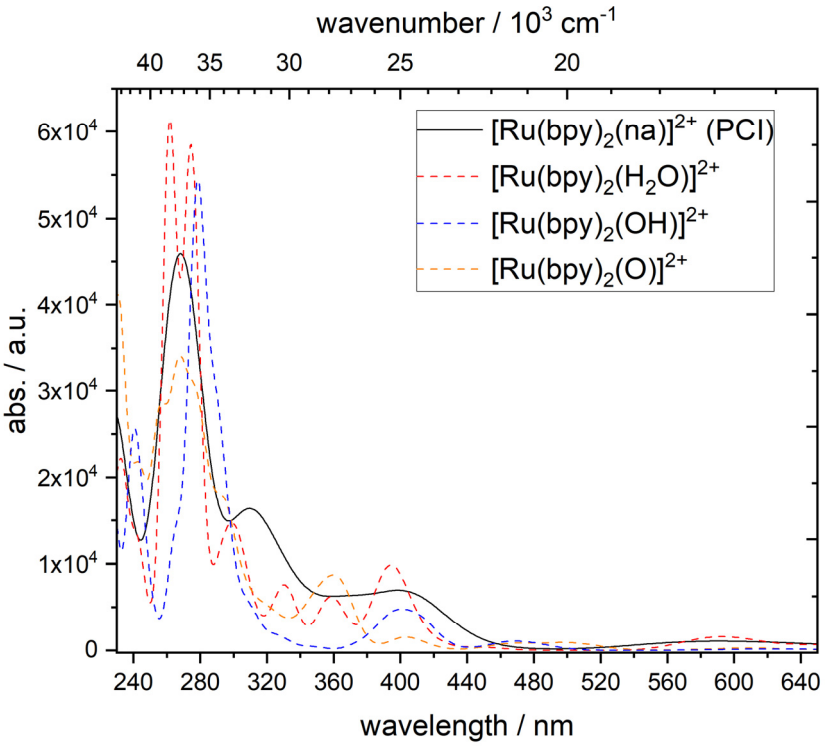

Figure 19 Calculated absorption spectra of $[Ru(bpy)_2(na)]^{2+}$ (PCI), $[Ru(bpy)_2(H_2O)]^{2+}$, $[Ru(bpy)_2(OH)]^{2+}$ and $[Ru(bpy)_2(O)]^{2+}$ obtained at the TD-DFT/B3LYP/cc-PVTZ level of theory (convoluted with 1500 cm^{-1} FWHM Gaussians).

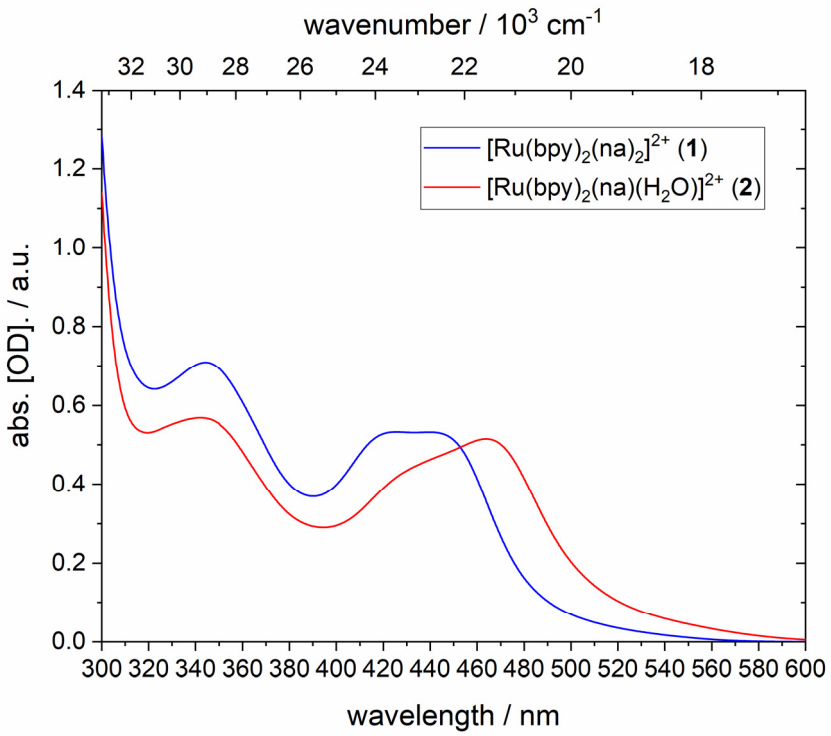

Figure 20 Static UV/Vis absorption spectrum of $[Ru(bpy)_2(na)_2]^{2+}$ (**1**) (blue) and $[Ru(bpy)_2(na)(H_2O)]^{2+}$ (**2**) (red) in H_2O.

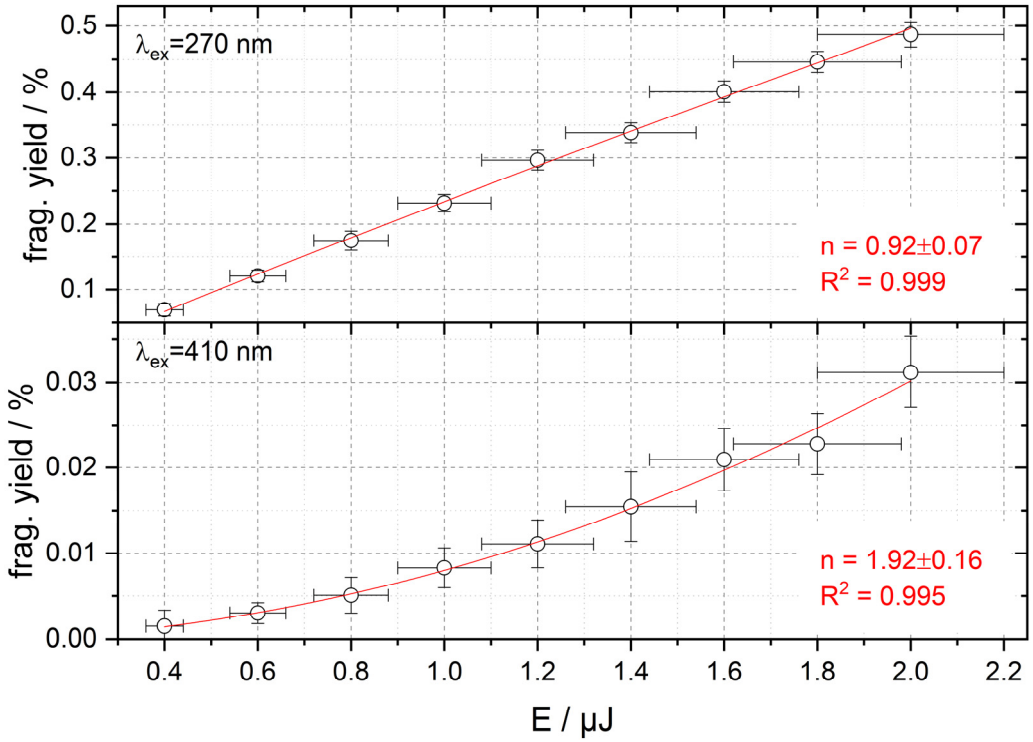

Figure 21 Laser pulse energy (*E*) dependence of total fragmentation yield *Y* of $[Ru(bpy)_2(na)_2]^{2+}$ (**1**) at λ_{ex} = 270 nm and 410 nm. Fitted to $Y = A * E^n$.

4. Ultrafast Transient Photodissociation Spectroscopy

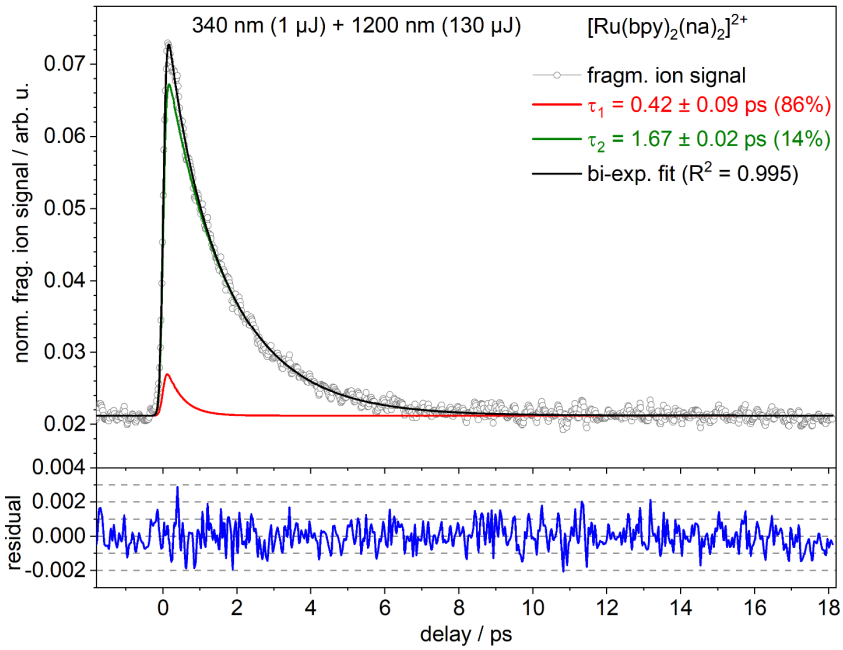

Figure 22 Normalized transient fragment ion intensity of $[Ru(bpy)_2(na)_2]^{2+}$ (**1**) recorded at λ_{pump} = 340 nm; bi-exponential fit (black) is given along the fit decomposition (green and red). Fit residual is shown below (blue).

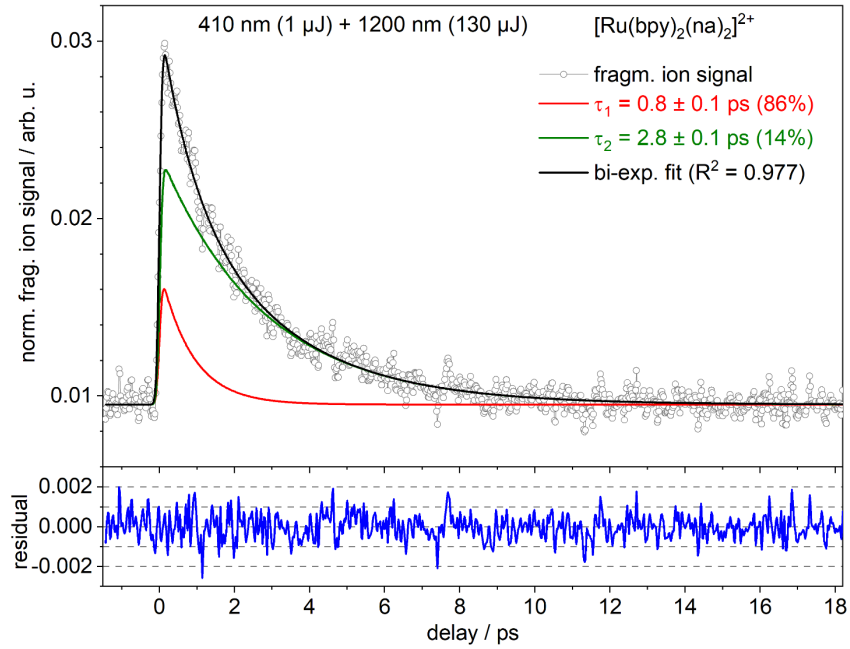

Figure 23 Normalized transient fragment ion intensity of $[Ru(bpy)_2(na)_2]^{2+}$ (**1**) recorded at λ_{pump} = 410 nm; bi-exponential fit (black) is given along the fit decomposition (green and red). Fit residual is shown below (blue).

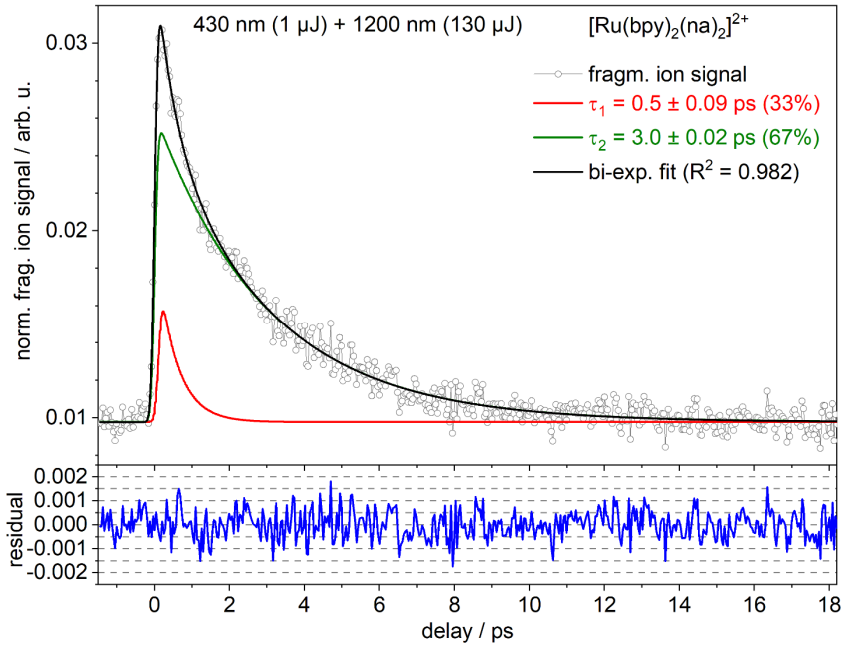

Figure 24 Normalized transient fragment ion intensity of $[Ru(bpy)_2(na)_2]^{2+}$ (**1**) recorded at λ_{pump} = 430 nm; bi-exponential fit (black) is given along the fit decomposition (green and red). Fit residual is shown below (blue).

5. Ultrafast Transient Absorption Spectroscopy

a) Global vs. local analysis

Due to the strongly convoluted difference spectra the global analysis was verified by a local multi-exponential analysis at 374, 425, 445, 475 and 675 nm for $[Ru(bpy)_2(na)_2]^{2+}$ (**1**) excited at 340 nm (flow cell) and at 370, 445, 465 and 675 nm for $[Ru(bpy)_2(na)(H_2O)]^{2+}$ (**2**) excited at 340 nm (rotating cell). For the local analysis five absorbance transients around the corresponding central wavelength were combined.
The resulting time constants and their corresponding amplitudes matched the global analysis results exceptionally well within the error limits as shown in SI-Tab. 3 and SI-Fig. 25 (cf. dots at 374, 425, 445, 475 and 675 nm (b) and 370, 445, 465 and 675 nm (d), representing the amplitudes of the local fits, matching the DAS of the global analysis).
Note that for **1** a fit with two instead of one time constant at 675 nm only leads to a minor and negligible improvement at early delay times. In addition, the fit then yields a short time constant of ~ 3.8 ps and not the (according to Greenough et al.[1]) expected ~ 0.3 - 0.4 ps. Thus, for our collected data no indication for a fast (~ 0.3 ps) rise of signal strength around 675 nm (possible 'PCI region') was found.

Table 3 Time constants resulting from a local analysis at a given wavelength compared to the global analysis of femtosecond transient absorption data in H_2O of $[Ru(bpy)_2(na)_2]^{2+}$ (**1**) excited at 340 nm (flow cell) and $[Ru(bpy)_2(na)(H_2O)]^{2+}$ (**2**) excited at 340 nm (rotating cell).

compound	analysis wavelength / nm	τ_1 / ps	τ_2 / ps	τ_3 / ps	τ_4 / ps
$[Ru(bpy)_2(na)_2]^{2+}$	374	0.3 ± 0.2	2.7 ± 0.4	15 ± 5	176 ± 6
	425	0.5 ± 0.3	3.7 ± 0.8	15 ± 7	182 ± 7
	445	/	3.0 ± 0.6	14 ± 7	181 ± 5
	475	/	3.5 ± 0.5	11 ± 3	176 ± 5
	675	/	/	/	188 ± 7
	global	0.29 ± 0.05	3.2 ± 0.2	12 ± 2	180 ± 10
$[Ru(bpy)_2(na)(H_2O)]^{2+}$	370	0.4 ± 0.3	2.8 ± 0.6	84 ± 5	
	445	0.5 ± 0.3	3.3 ± 0.3	80 ± 3	
	465	0.5 ± 0.2	2.8 ± 0.3	79 ± 3	
	675	0.5 ± 0.1	/	80 ± 3	
	global	0.6 ± 0.1	3.0 ± 0.3	83 ± 5	

/: component of global analysis not found in local analysis at the corresponding wavelength.

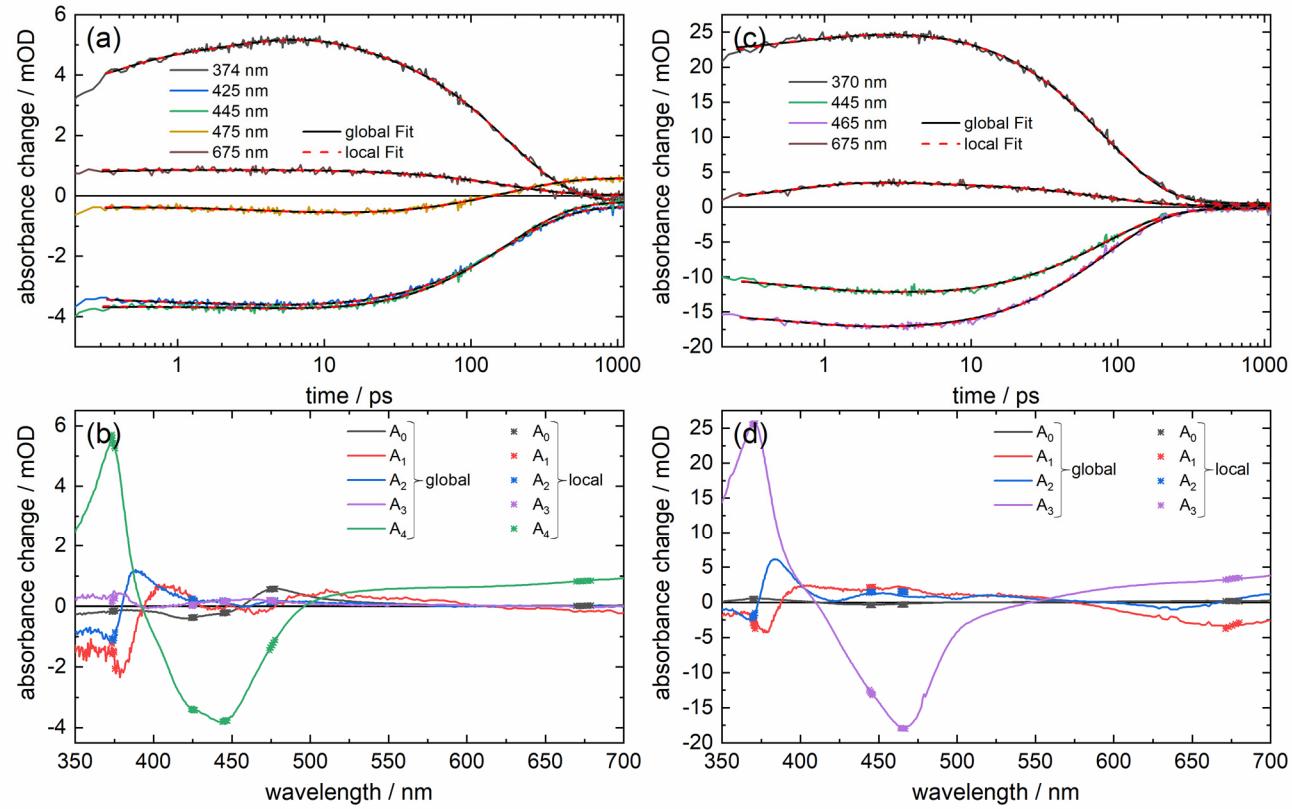

Figure 25 Comparison of local and global analysis results: Fits of absorbance transients at selected wavelengths (a), (c), amplitudes and decay associated spectra (DAS) (b), (d) for $[Ru(bpy)_2(na)_2]^{2+}$ (**1**) in H_2O, excited at 340 nm in a flow cell (a), (b) and for $[Ru(bpy)_2(na)(H_2O)]^{2+}$ (**2**) in H_2O, excited at 340 nm in a rotating cell (c), (d). Corresponding time constants are given in SI-Tab. 3.

Solid black line in (a), (c): Results of a global analysis according to eq. (2); dashed red line in (a), (c): Results of a local analysis according to eq. (2).

Solid lines in (b), (d): Resulting DAS of a global analysis according to eq. (2); dots in (b), (d): Resulting amplitudes of a local analysis according to eq. (2).

b) Cross check for number of slow time constants for $[Ru(bpy)_2(na)_2]^{2+}$ (1) in H_2O: Fit with a forced, additional 155 ps component

Based on the given rate model and the determined time constants[A] in model G[1] a calculation of the corresponding 'theoretical apparent' time constant for the 'caged PCI-(na)-pair' yields 155 ps ($^1/_\tau = {}^1/_{\tau_{GR}} + {}^1/_{\tau_S}$, GR: geminate recombination, S: diffusional separation), which, according to model G[1], should be found alongside the 180 ps by a global analysis.

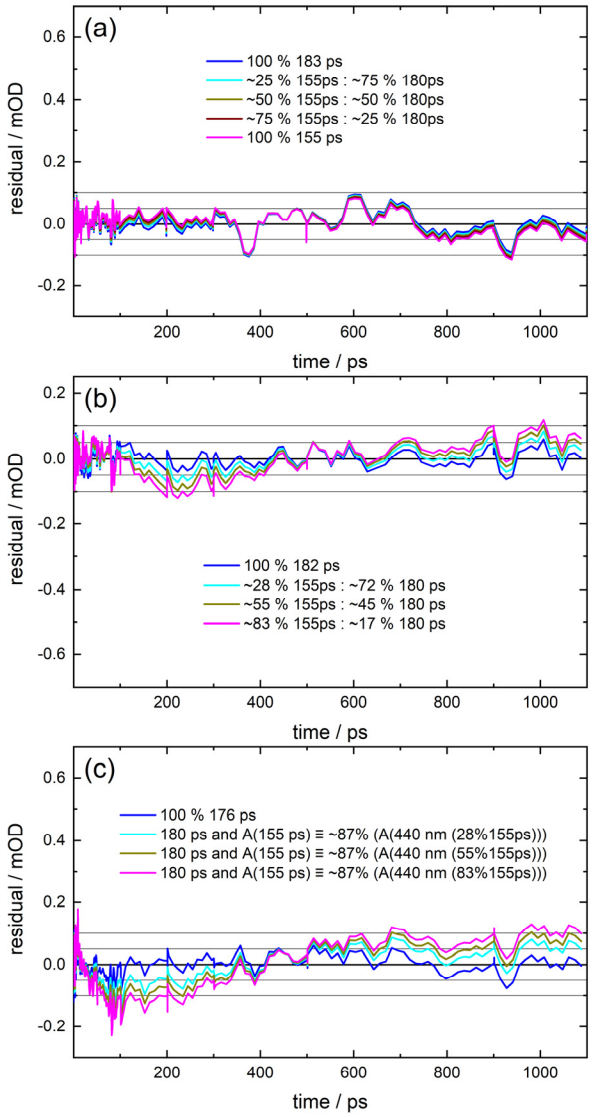

Figure 26 Comparison of fit residuals of averaged absorbance transients around 675 nm ('PCI') (a), 440 nm (GSB) (b) and 374 nm (^{3}MLCT-ESA and GSB) (c) for $[Ru(bpy)_2(na)_2]^{2+}$ (**1**) in H_2O excited at 340 nm (flow cell) with a free fit of a single longer component (blue line) and different ratios for a forced fit of a 155 and a 180 ps component (more details in the text).

Even as the local fits of our collected data yields solely ~ 180 ps as a slow time constant for $[Ru(bpy)_2(na)_2]^{2+}$ (**1**) (see above), a (superimposed) contribution of a 155 ps component cannot be excluded in the first place due to the small difference between 155 and 180 ps. According to model G[1] the 155 ps component should occur with different sign and amplitude in different wavelength regions: (i) in both the ^{3}MLCT ESA-region around 374 nm and in the GSB region as ground state recovery (with negative amplitude) and (ii) in the longer wavelength region above 650 nm as ESA-decay (with positive amplitude). Following the quantum yields given in model G[1B], in the region of GSB (GSR) the ratio of the 155 to the 180 ps component comes to ~ 83 % : ~ 17 %. Thus, the GS recovery around 440 nm should be dominated by the 155 ps component. For wavelengths above 650 nm exclusively the 155 ps component should be found, as only contributions of the PCI were assumed in this region. Thus, as a cross check a corresponding local fit with a forced additional 155 ps time constant was performed for **1**, excited at 340 nm (flow cell). Note that the amplitudes (and the time constant) for the 155 ps component had to be fixed for all fits, else the returned amplitudes were small compared to the 180 ps component and (more relevant) had the wrong sign and thus they were not physically reasonable. For the region around 374 nm the absorbance transients from 364 to 384 nm were averaged and a 3-point moving average over the collected time points was applied to improve the signal-to-noise-ratio. Analogous averages were performed for 440 nm (435 to 445 nm) and for 675 nm (650 to 700 nm).

Above 650 nm a forced fit with 155 ps reduced the quality of the fit (and accordingly the fit residual in SI-Fig. 26a) only in a small extent compared to the low signal-to-noise ratio. Thus, a participation of a 155 ps component cannot be completely excluded there. However, the residual becomes larger for larger amplitudes of the 155 ps component, and a free fit (without fixing the time constant to 155 ps) always results in ~ 180 ps, rendering a mere 155 ps time constant unlikely.

In the region of the GSB (and the ^{3}MLCT ESA) a forced fit with a 155 ps component clearly reduced the fit quality: the more the ratio of the amplitudes is shifted towards the 155 ps component, the larger is the fit residual (cf. SI-Fig. 26b). A forced ratio of ~ 83 % : ~ 17 % for the two components leads to a significantly worse fit as a fit with only the 180 ps component and can therefore be excluded as a valid fit for our data. The same applies for the 374 nm region. The free fit with solely 176 ps shows a very good result (cf. SI-Fig. 26c). Increasing the forced contribution of the 155 ps component up to the extent given by model G[1], increases the residual significantly. The extent given by

[A] Greenough et al.[1] applied a 'target analysis' approach instead of a global analysis approach. A rate model along with spectral amplitudes for each species was proposed and the data analysis was performed according to these amplitudes with the differential equations corresponding to the rate model. Thereby, kinetic traces for the different species of the rate model were extracted and the rate constants were obtained. The time constant for VR in the ^{3}MLCT state of 3.6 ps was obtained through a fit in the (integrated) absorbance transients of the red edge of the UV ^{3}MLCT band and fixed during the 'target analysis'.

[B] Quantum yields according to Greenough et al.[1]: $\phi_{^3MLCT(v=0)}$ = 0.11 , ϕ_{GR}= 0.53. Thus, the (overall 64 % for) GSR is the sum of 11% ^{3}MLCT-GS-recovery (with 180 ps) and 53 % through geminate recombination from the PCI (with 155 ps) in a ratio of ~ 17 % : ~ 83 % for the amplitude ratio of the 180 and 155 ps component, and the residual 36 % represented by formation of $[Ru(bpy)_2(na)(H_2O)]^{2+}$ (**2**).

model G[1] is dertermined by the already calculated contribution at 440 nm, scaled to the relative extinction (i.e. 87 %) of the GS spectrum of **1** at 374 nm.

c) Estimation of quantum yield for product $[Ru(bpy)_2(na)(H_2O)]^{2+}$ (2) from educt $[Ru(bpy)_2(na)_2]^{2+}$ (1), and simulation of the 1090 ps difference spectrum by static absorption spectra of product 2 and educt 1

A direct determination of the quantum yields from the fs TA data for $[Ru(bpy)_2(na)_2]^{2+}$ (**1**) in solution is not possible. To roughly estimate a quantum yield for product **2** from educt **1**, three different scenarios were examined.
For all scenarios the spectral region of the ground state bleach signal of the flow cell measurement on **1** in H_2O excited at 340 nm was investigated and the influence of the superimposed ^{3}MLCT-ESA-signals on both ends of its spectral range was neglected. For the analysis of the difference spectra $y(t)$ were written as

$$y(t) = [x_2(t) \cdot S_2 - x_1(t) \cdot S_1]\, a(t) \qquad \text{eq. (SI-1)}$$

with scaling factors $x_1(t)$ and $x_2(t)$ for the contributing static UV/Vis absorption spectra (Fig. 4) of **1** (termed S_1 onward) and of **2** (termed S_2 onward), respectively and a general scaling factor $a(t)$. The analyses were performed for very early delay time (0.3 ps) and for late delay time (1090 ps).

Scenario (i): (na)-dissociation and (H_2O) ligation are completed within system response (Model B).
Accordingly, the difference spectra $y(t)$ at t = 0.3 and 1090 ps were simulated via eq. (SI-1) (cf. SI-Fig. 27a), yielding the quantum efficiency for **2** $\phi_{(2)}$ = 1- $\phi_{(1)}$ = 1 - (3.7 - 1) / 3.7 = 27 %.

Scenario (ii): As in Scenario (i) (na)-dissociation and (H_2O) ligation are completed within system response (Model B). However, here an upper limit for $\phi_{(2)}$ is derived from the shape of the red edge of the GSB at early delay times.
To this end an upper limit for the extent of product **2** at early delay times (0.3 ps) was determined by quantitatevly evaluating the extent of spectral narrowing (with respect to the static ground state spectrum of **1**) of the low energetic part of the (negative) GSB, as caused by the superimposed (positive) band of product **2**.
Accordingly, exclusively the red flank (445 – 480 nm) of the difference spectrum $y(t)$ at t = 0.3 ps was simulated via eq. (SI-1) (cf. SI-Fig. 27b), yielding the quantum efficiency for **2** $\phi_{(2)}$ = 1- $\phi_{(1)}$ = 1 - (4.3 – 1.5) / 4.3 = 35 %.

Scenario (iii): Slow formation of product **2** (model A), i.e. no product at at early delay times (0.3 ps), but completed product formation at late delay times (1090 ps).
Accordingly, the difference spectra $y(t)$ at t = 0.3 and 1090 ps were simulated via eq. (SI-1) (cf. SI-Fig. 27c), yielding the quantum efficiency for **2** $\phi_{(2)}$ = 1- $\phi_{(1)}$ = 1 - (2.9 - 1) / 2.9 = 34 %.

In Summary, it is interesting to note, that the three scenarios yield very similar values for $\phi_{(2)}$ (27 – 35%) for both model A (slow formation of **2**) and B (ultrafast formation of **2**). Moreover, these values are as well consistent with $\phi_{(2)}$ reported in model G.[1]

Simulation of the 1090 ps difference spectrum by static absorption spectra of educt **1** and product **2**:
As mentioned in the main text, the difference spectrum for **1** in H_2O at 1090 ps can be simulated according to eq. (SI-1) in excellent agreement (cf. SI-Fig. 27a, c, blue and green lines), confirming the assignment of the band around 475 nm at long delay times to the photoproduct **2**.

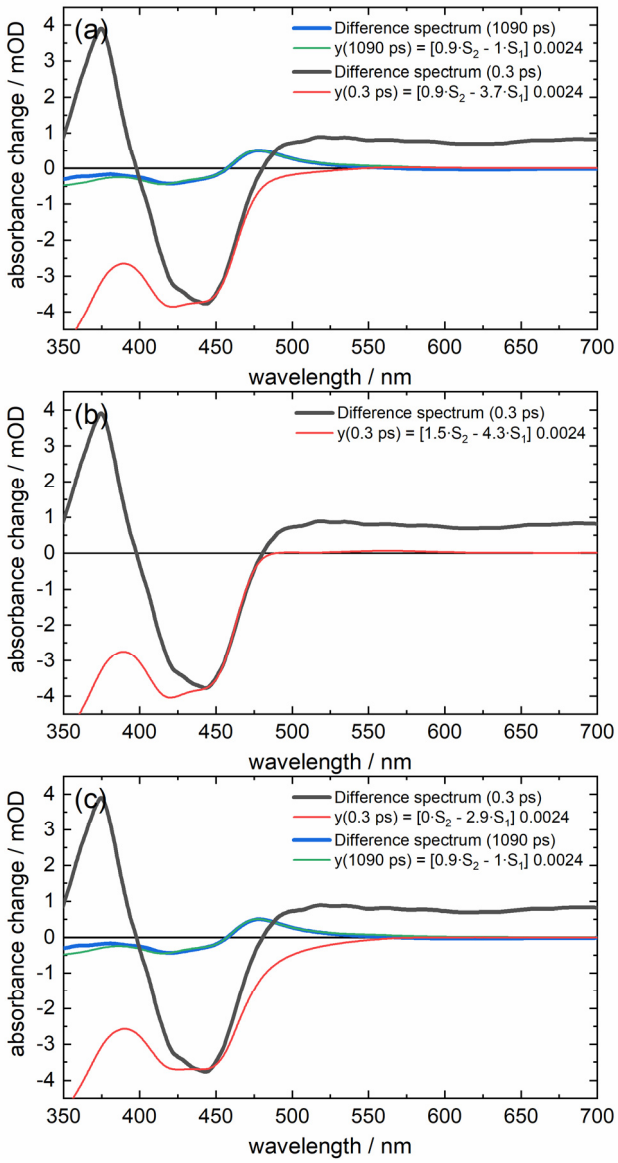

Figure 27 Simulation of the difference signals in the GS bleach region of $[Ru(bpy)_2(na)_2]^{2+}$ (**1**) in H_2O (excited at 340 nm, flow cell) at 0.3 and 1090 ps for estimation of the quantum yield of product (**2**) in scenario (i) viz. rapid product formation as in model B (a), (ii) as upper limit via the shape of the red edge of the GSB at early delay times (b), and (iii) viz. slow product formation as in model A (c). More details in the text.
Bold lines: Difference spectra, thin lines: Simulations according to eq. (SI-1) and scenarios (i) - (iii).

d) Static UV/Vis absorption spectra of $[Ru(bpy)_2(na)_2]^{2+}$ (1), $[Ru(bpy)_2(na)(H_2O)]^{2+}$ (2) and $[Ru(bpy)_2(H_2O)_2]^{2+}$ via an irradiation series

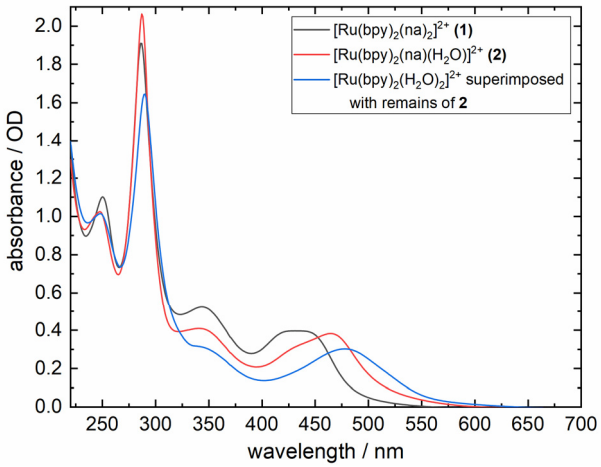

Figure 28 Static UV/Vis absorption spectrum of $[Ru(bpy)_2(na)_2]^{2+}$ (**1**, grey line), $[Ru(bpy)_2(na)(H_2O)]^{2+}$ (**2**, red line) and $[Ru(bpy)_2(H_2O)_2]^{2+}$ superimposed with remains of **2** (blue line) in H_2O. The spectra are part of a static series where the photoproducts of **1** were generated by irradiating a fresh sample of **1** in H_2O with ~20 mW 465 nm pulsed light generated by the TOPAS described in main text (Methods - Liquid phase experiments). The spectrum of **2** was obtained after ~ 5.5 min irradiation and further irradiation of the sample for 3 h yielded the blue line spectrum. Further irradiation led to a slow decrease in signal strength in the MLCT bands (around 475 nm) concomitant with a broadening around 315 nm at the red edge of the LC band. Thus, on long time scales the formation of $[Ru(bpy)_2(H_2O)_2]^{2+}$ from **2** could be limited by a decomposition of the complex, and the reported spectra[1] of $[Ru(bpy)_2(H_2O)_2]^{2+}$ was not obtained here. The same behavior was observed for an analogue series under irradiation with 365 nm continuous light from a ~ 15 mW LED, where **2** was obtained after ~ 60 s and the effect of complex-decomposition afterwards was larger.

Note that the here observed formation of photoproducts from **2** was not observed in the consecutive measurement cycles of the fs time resolved measurements on **2**, where no change of the absorption spectrum as shown in Fig. 4 was observed after five cycles. As well, storage of a sample of **2** in ambient light does not significantly change the absorption spectrum of the sample towards $[Ru(bpy)_2(H_2O)_2]^{2+}$ after two days. Thus, both the formation of $[Ru(bpy)_2(H_2O)_2]^{2+}$ and the complex-decomposition observed here require high doses of light and are very slow compared to the formation of **2** from **1** (i.e. they are negligible for the time resolved measurements presented).

e) Decay associated spectra (DAS) behavior in case of a faster succeeding step ('$k_2 > k_1$')

A positive DAS component can (counter-intuitively) indicate the formation of a state instead of its decay, if the faster kinetic step follows a slower one, as described in the main text for A_3 of $[Ru(bpy)_2(na)_2]^{2+}$ (**1**) in H_2O. This general behavior is illustrated in the following.

For simplicity a scheme with 3 consecutive states A, B and C as shown in SI-Scheme 1 is considered.

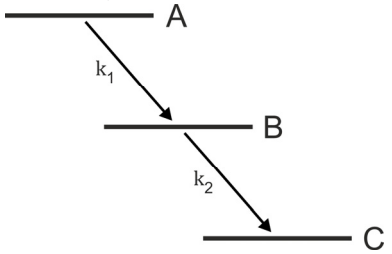

Scheme 1 Simplified scheme for three sequential states A, B and C with the respective rates k_1 and k_2.

The rate system for the concentrations c_i (i = A, B, C) is given by eq. (SI-2) and the boundery conditions $c_A(0) \equiv 1$ and $c_A(t) + c_B(t) + c_C(t) = \sum_i c_i(t) \equiv 1$:

$$\begin{aligned} \frac{\mathrm{d}c_A}{\mathrm{d}t} &= -k_1 c_A \\ \frac{\mathrm{d}c_B}{\mathrm{d}t} &= k_1 c_A - k_2 c_B \\ \frac{\mathrm{d}c_C}{\mathrm{d}t} &= k_2 c_B \end{aligned} \qquad \text{eq. (SI-2)}$$

Generalized the solution for N states can be written as eq. (SI-3a) and in the simplified case here as eq. (SI-3b,c), where c_N is the ground state, which is the only populated state prior and after the measurement.

$$c_i(t) = \sum_{j=1}^{N} a_{ij} e^{-k_j t} + b_i \qquad \text{eq. (SI-3a)}$$

$$c_i(t) = \sum_{j} a_{ij} e^{-k_j t} \quad \text{for } i < N \qquad \text{eq. (SI-3b)}$$

$$c_N(t) = \sum_{j} a_{Nj} e^{-k_j t} + b_N \quad \text{with } k_N = 0 \quad \text{and } b_N = 1 \text{ for } \sum_j c_j = 1 \qquad \text{eq. (SI-3c)}$$

The absorbance change ΔOD, which is measured here, is given as difference between the absorbance of the excited ($A(\lambda, t)$) and the unexcited ($A_0(\lambda)$) sample. With $A(\lambda, t) = \sum_i c_i(t)\varepsilon_i(\lambda)$ and $A_0(\lambda) = \varepsilon_N(\lambda)$ ($\varepsilon_i(\lambda)$: extinction coefficient of the state i, optical path length $d \equiv 1$) ΔOD can then be written as:

$$\Delta OD(\lambda, t) = A(\lambda, t) - A_0(\lambda) = \varepsilon_N(\lambda) + \sum_i \sum_j a_{ij} e^{-k_j t} \varepsilon_i(\lambda) - \varepsilon_N(\lambda) = \sum_j \left[\sum_i a_{ij} \varepsilon_i(\lambda) \right] e^{-k_j t} \qquad \text{eq. (SI-4)}$$

Alternetively, eq. (SI-4) can be rewritten in the form of the global multi-exponential fit function eq. (2):

$$\Delta A(\lambda, t) \left(= \Delta OD(\lambda, t)\right) = A_0(\lambda) + \sum_{j=1}^{N} A_j(\lambda)\, e^{-t/\tau_j} \quad \text{with } \tau_j = 1/k_j \quad \text{and } A_j(\lambda) = \sum_i a_{ij} \varepsilon_i(\lambda). \qquad \text{eq. (2)}$$

for the simplified case here: $A_0(\lambda) = \varepsilon_N(\lambda) - \varepsilon_N(\lambda) = 0$

Here the DAS $A_j(\lambda)$ appear as coefficients $a_{ij}\varepsilon_i(\lambda)$ of the linearly combined exponential terms e^{-t/τ_j}. For the example with the states A, B and C the simple solution for eq. (SI-2) yields the a_{ij} and thus the $A_j(\lambda)$ as:

$$\begin{aligned} A_0(\lambda) &= 0 \\ A_1(\lambda) &= \varepsilon_A(\lambda) + \frac{k_1}{k_2 - k_1}\varepsilon_B(\lambda) + \frac{k_2}{k_1 - k_2}\varepsilon_C(\lambda) \\ A_2(\lambda) &= \frac{k_1}{k_1 - k_2}\varepsilon_B(\lambda) + \frac{k_1}{k_2 - k_1}\varepsilon_C(\lambda) \end{aligned} \qquad \text{eq. (SI-5)}$$

Obviously, the signs of the coefficients of $\varepsilon_B(\lambda)$ and $\varepsilon_C(\lambda)$ depend on k_1 and k_2.
For $k_2 > k_1$ (e.g. for the rate constants $k_1 = 1/180\ ps$ and $k_2 = 1/12\ ps$ as described in the main text) eq. (SI-5) yields:

$$\begin{aligned} A_0(\lambda) &= 0 \\ A_1(\lambda) &= \varepsilon_A(\lambda) + 0.07 \cdot \varepsilon_B(\lambda) + (-1.07) \cdot \varepsilon_C(\lambda) \\ A_2(\lambda) &= (-0.07) \cdot \varepsilon_B(\lambda) + 0.07 \cdot \varepsilon_C(\lambda) \end{aligned} \qquad \text{eq. (SI-6)}$$

Here, as the main result, $A_2(\lambda)$ is not only small compared to A_1, but most importantly the absorption spectrum of C ($\varepsilon_C(\lambda)$) appears as positive contribution even though it represents the state which gets populated. Correspondingly, the intermediate state B contributes to $A_2(\lambda)$ with negative sign.
$A_1(\lambda)$ is only slightly modulated compared to a direct transition from A to C ($A_1(\lambda) = \varepsilon_A(\lambda) - \varepsilon_C(\lambda)$) by a small contribution (+0.07) due to the short lived intermediate state B, and a contribution of -1.07 instead of -1.0 for state C.

In reference to $[Ru(bpy)_2(na)_2]^{2+}$ (**1**) in H_2O, $A_2(\lambda)$ as derived in eq. (SI-6) is the equivalent to $A_3(\lambda)$ found for **1**. As described in the main text, the positive amplitude $A_3(\lambda)$ is identified with the formation of **2** and of the ground state of **1** via the short lived PCI, instead of a depletion of a state. Note that this simplified example neglects the composite character of the rate constants, e.g. the formation of two final states (ground state of **1** and of **2**). However, even when thereby the mathematics gets more complicated, the qualitative result remains the same, i.e. the counter-intuitive reversal of the sign of A_3 with respect to a sequence with decreasing instead of increasing rates.

f) Detailed survey and discussion of the literature regarding main aspects of model A and B for $[Ru(bpy)_2(na)_2]^{2+}$ (1) and $[Ru(bpy)_2(na)(H_2O)]^{2+}$ (2) in H_2O

In what follows, we discuss some important aspects of our models A and B for $[Ru(bpy)_2(na)_2]^{2+}$ (**1**) and $[Ru(bpy)_2(na)(H_2O)]^{2+}$ (**2**) in H_2O, as described in the main text, in light of the broader, highly diverse literature on the photochemistry of Ru^{II}-polypyridine complexes.

Time Scales. Quite diverse time scales for dissociation and product formation have been reported. Analogue to model G,[1] rapid (< 10 ps) dissociation and slow (77 ps) ligation was suggested for $[Ru(bpy)_2(CH_3CN)_2]^{2+}$.[4] However, for $[Ru(1\text{-isocyTPQA})(CH_3CN)_2]^{2+}$ both ultrafast or slow pathways were considered possible for photoproduct formation,[5] as we do here for **1** and **2**. Fast dissociation (as in model B) is generally reported for (sterically not hindered) CO ligands (small compared to na), along with rapid or with slower photoproduct formation in solution.[6-10] Slow dissociation (42 ps) was considered for CH_3CN.[5] For ligand isomerization via a dissociative process a fast (< 10 ps) and a slow (580 ps) pathway was reported.[11] Slow (ns-regime) py-H_2O exchange reaction was reported for $[Ru(bpy)_2(py)_2]^{2+}$ in H_2O.[12]

By introducing the dissociation as (slow) time determining step (τ_4 = 180 ps) for photoproduct formation of **1** in model A, τ_3 = 12 ps becomes a possible time scale for solvent H_2O-ligation alongisde na separation (and geminate recombination) as succeeding fast step, which is in accordance with quantum chemical simulations predicting H_2O-ligation in a range less than 10 ps.[13] This hydrophilicity is also in line with the observation of spontaneous attachment of H_2O on PCI in our gas phase experiments.

Participation of several ^{3}MLCT states and coupling to ^{3}MC states. The implementation of several ^{3}MLCTs has been reported extensively in the literature,[11, 14-20] and is here motivated by the need for a kinetic decoupling of ^{3}MLCT deactivations pathways (VR) as observed via A_1 and A_2. Their existence is in accordance with our DFT calculations (cf. below), predicting several energetically close ^{3}MLCT states with either bpy or na character.

The coupling of ^{3}MLCT with ^{3}MC states[14, 19-23] allows various kinetic scenarios, such as an equilibrium[12, 14, 22-24] as proposed for **1** and **2** in this work. However, a possible equilibrium or a more consecutive course depends on the magnitudes of the rates involved: As shown for $[Ru(tpy)_2]^{2+}$ and $[Ru(ttpy)_2]^{2+}$, the time determining rate for GSR can be (i) the rate for ISC from ^{3}MC (in a fast equilibrium with ^{3}MLCT) to ^{1}GS ($[Ru(tpy)_2]^{2+}$) or (ii), in a more consecutive scheme, the rate for IC from ^{3}MLCT to ^{3}MC ($[Ru(ttpy)_2]^{2+}$), followed by faster GSR.[22] For **1** besides case (i), as proposed here, case (ii) is as well possible and IC from the relaxed ^{3}MLCT state to the ^{3}MC state might be the time determining process, followed by faster GSR (and dissociation in model A). But for **2** a signal rise in the ^{3}MC region (> 550 nm) with 0.6 ps along with GSR via solely one apparent time constant (83 ps) was observed, and consequently case (ii) can be excluded due to kinetic reasons. Therefore, we prefer the equilibrium model to the consecutive model.

The long wavelength region (> 550 nm) is proposed as ^{3}MC region in analogy to literature[25-27] (see main text) and represents the ^{3}MC state in equilibrium with the ^{3}MLCT state in model A and B ($^3MC_{hexa}$). An additional state ^{3}MC' is required in model B to decouple the relaxation pathways (fast dissociation and GSR) and is not time-resolved. Thus, in this picture at least two ^{3}MC states[11, 20, 28-30] have to participate in the photoinduced dynamics of **1** and **2**.

While one of the ^{3}MCs in model B recovers slowly to ^{1}GS, the other (^{3}MC') leads to rapid ligand dissociation. For this rapid dissociation the ^{3}MC' has to be populated within the system response from a third participating ^{3}MLCT or directly from ^{1}MLCT (see main text). The same applies in model A and B for the rapid population of the $^3MC_{hexa}$ of **1**, forming the equilibrium with ^{3}MLCT (dashed blue arrow in Fig. 8a). In conflict to the generally assumed near unity quantum yield ISC from ^{1}MLCT to ^{3}MLCT states, a direct population of ^{3}MC from ^{1}MLCT states has in fact been considered possible for this class of molecules.[14, 20, 31, 32]

6. Theoretical Analysis

a) Bonding disscociation energy

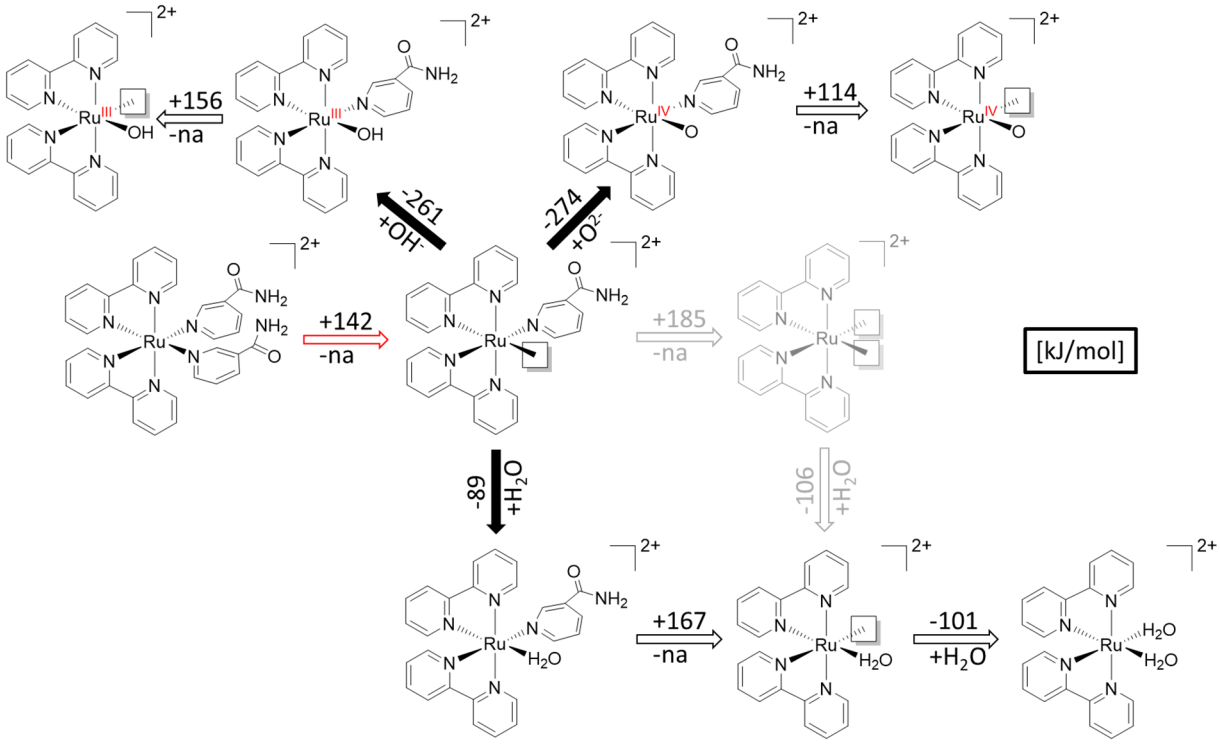

Figure 29 Calculated bond energy of the different dissociation pathways of $[Ru(bpy)_2(na)_2]^{2+}$ (**1**). B3LYP/cc-PVTZ/MDF28 (Stuttgart97) including zero-point energy correction.

b) TD-DFT excited state calculation and characterization of the excited states

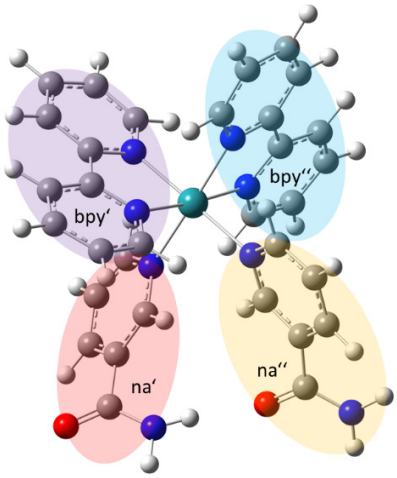

Figure 30 Structural elements of the $[Ru(bpy)_2(na)_2]^{2+}$ (**1**) complex.

Table 4 Calculated transitions of $[Ru(bpy)_2(na)_2]^{2+}$ (**1**) at the ground state geometry (TD-DFT/B3LYP/cc-PVTZ). The singlet transitions with an oscillator strength of f > 0.03 are displayed and major contributions to electronic transitions with a weight of ≥ 10%. Only calculated triplet states in the area of 420 nm and 340 nm are displayed and major contributions to electronic transitions with a weight of ≥ 40%.

State	λ_{cal} [nm]	E_v [eV]	*f*	Transitions	Weight [%]	Involved ligands/metals	Transition type
T_6	463.6	2.67	-	H-2→L+1	86	Ru → bpy''	MLCT
S_5	439.6	2.82	0.084	H-2→L H-1→L+1	59 22	Ru → bpy' Ru → bpy''	MLCT
S_6	426.0	2.91	0.050	H-2→L H-1→L+1 H →L+1	25 45 12	Ru → bpy' Ru → bpy'' Ru → bpy''	MLCT
T_7	413.0	3.00	-	H →L+11	71	Ru → Ru	MC
T_8	408.3	3.04	-	H-2→L+2	68	Ru → na'	MLCT
S_{12}	362.0	3.43	0.041	H-2→L+2	82	Ru → na'	MLCT
S_{15}	346.8	3.58	0.047	H-2→L+3	71	Ru → na', bpy'	MLCT
T_{27}	343.3	3.61	-	H-2→L+4	28	Ru → na'	MLCT
T_{28}	340.7	3.64	-	H-2→L+4 H-2→L+5	38 23	Ru → na' Ru → na', na''	MLCT
T_{29}	338.9	3.66	-	H →L+5	32	Ru → na', na''	MLCT
T_{30}	337.1	3.68	-	H →L+7	50	Ru → bpy', bpy''	MLCT
S_{25}	326.1	3.80	0.034	H-2→L+5 H-2→L+6 H-1→L+7 H →L+7	15 18 12 26	Ru → na', na'' Ru → na' Ru → bpy', bpy'' Ru → bpy', bpy''	MLCT
S_{26}	325.4	3.81	0.035	H-2→L+5 H-1→L+5 H →L+7	45 10 15	Ru → na', na'' Ru → na', na'' Ru → bpy', bpy''	MLCT
S_{50}	279.9	4.43	0.048	H-5→L+1 H-3→L+7 H-3→L+8 H-1→L+9	15 20 18 14	bpy'' → bpy'' na'' → bpy', bpy'' na'' → na'', bpy'' Ru → na''	ILCT
S_{52}	278.9	4.45	0.056	H-7→L H-6→L+1 H-3→L+7 H-2→L+9 H-1→L+9	14 21 10 11 13	bpy' → bpy' na' → bpy'' na'' → bpy', bpy'' Ru → na'' Ru → na''	ILCT MLCT
S_{54}	276.9	4.48	0.098	H-7→L H-3→L+3 H-3→L+8	22 19 36	bpy' → bpy' na'' → na', bpy' na'' → na'', bpy''	LC
S_{55}	275.7	4.50	0.078	H-5→L+1 H-4→L+4 H-2→L+9	10 17 18	bpy'' → bpy'' NH_2''→ na', na'' Ru → na''	-
S_{56}	275.4	4.50	0.033	H-8→L+1	79	na'' → bpy''	ILCT
S_{57}	274.7	4.51	0.313	H-7→L H-5→L+1 H-4→L+4	19 25 14	bpy' → bpy' bpy'' → bpy'' NH_2''→ na', na''	LC
S_{73}	247.7	5.01	0.034	H-7→L+3	62	bpy' → na', bpy'	LC
S_{98}	229.2	5.41	0.053	H-11→L+1 H-5 →L+8	20 35	na' → bpy'' bpy'' → na'', bpy''	ILCT
S_{100}	228.5	5.43	0.033	H-10→L+2	51	na' → na'	LC

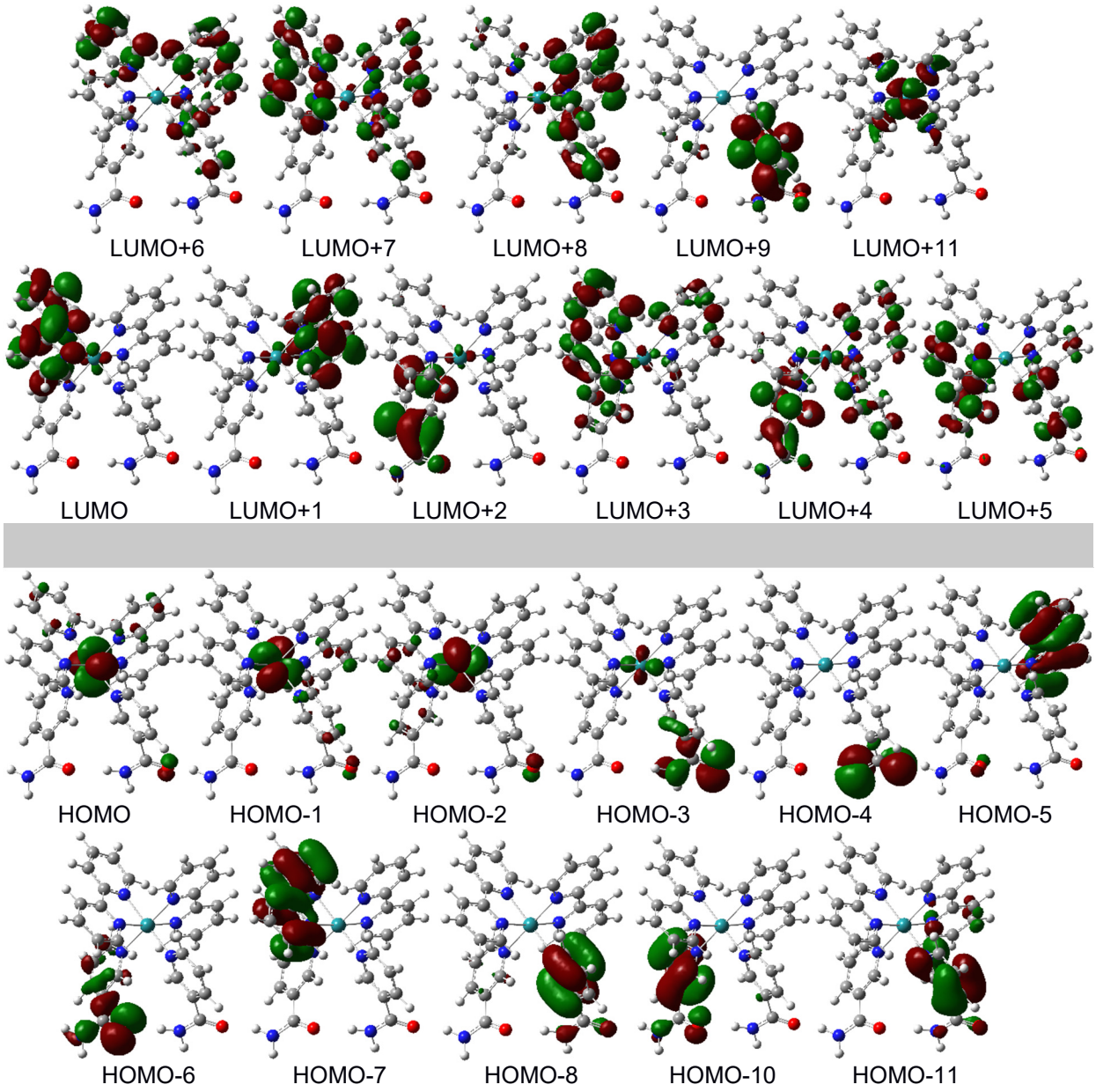

Figure 31 Molecular orbital isosurfaces of $[Ru(bpy)_2(na)_2]^{2+}$ (**1**), contributed to electronic transition with a weight of < 10%.

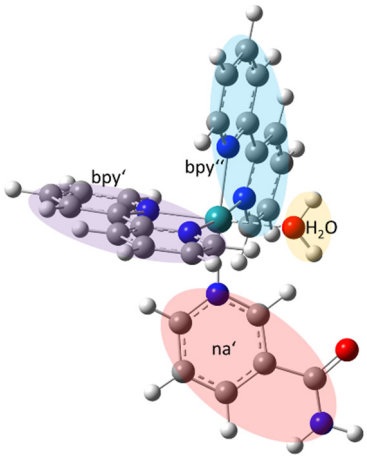

Figure 32 Structural elements of the $[Ru(bpy)_2(na)(H_2O)]^{2+}$ (**2**) complex.

Table 5 Calculated transitions of $[Ru(bpy)_2(na)(H_2O)]^{2+}$ (**2**) at the ground state geometry (TD-DFT/B3LYP/cc-PVTZ). The singlet transitions with an oscillator strength of f > 0.02 are displayed and major contributions to electronic transitions with a weight of ≥ 10%. Only calculated triplet states in the area of 420 nm and 340 nm are displayed and major contributions to electronic transitions with a weight of ≥ 8%.

State	λ_{cal} [nm]	E_v [eV]	*f*	Transitions	Weight [%]	Involved ligands/metals	Transition type
T_7	467.0	2.65	-	H-2→L H-1→L H-1→L+1	30 12 24	Ru → bpy‘, bpy‘‘ Ru → bpy‘, bpy‘‘ Ru → bpy‘, bpy‘‘	MLCT
T_8	449.8	2.76	-	H-1→L H-1→L+8 H →L+8	13 32 17	Ru → bpy‘, bpy‘‘ Ru → Ru, H_2O Ru → Ru, H_2O	MC, MLCT
S_5	427.1	2.90	0.107	H-2→L H-1→L+1	72 16	Ru → bpy‘, bpy‘‘ Ru → bpy‘, bpy‘‘	MLCT
T_9	426.2	2.91	-	H-2→L H-2→L+8	18 47	Ru → bpy‘, bpy‘‘ Ru → Ru, H_2O	MC, MLCT
T_{10}	411.0	3.02	-	H →L+2 H →L+3	56 10	Ru → na’ Ru → bpy’	MLCT
S_6	407.3	3.04	0.040	H-2→L+1	71	Ru → bpy‘, bpy‘‘	MLCT
T_{20}	345.5	3.59	-	H-2→L+6 H →L+5 H →L+6	14 29 23	Ru → bpy‘, bpy‘‘ Ru → bpy‘, bpy‘‘ Ru → bpy‘, bpy‘‘	MLCT
T_{21}	344.4	3.60	-	H-2→L+2 H →L+4	11 51	Ru → na’ Ru → na’, bpy‘	MLCT
T_{22}	342.2	3.62	-	H-2→L+2 H-2→L+10 H →L+4	16 20 15	Ru → na’ Ru → Ru Ru → na’, bpy‘	MLCT, MC
T_{23}	338.1	3.67	-	H-2→L+3 H →L+5 H →L+6	14 26 29	Ru → bpy’ Ru → bpy‘, bpy‘‘ Ru → bpy‘, bpy‘‘	MLCT
T_{24}	335.3	3.70	-	H-3→L+2 H-1→L+4	33 13	NH_2 → na’ Ru → na’, bpy‘	ILCT
S_{11}	352.8	3.51	0.071	H-2→L+2 H-1→L+2 H →L+2	10 29 32	Ru → na’ Ru → na’ Ru → na’	MLCT
S_{23}	315.7	3.93	0.038	H-1→L+6 H →L+7	19 65	Ru → bpy‘, bpy‘‘ Ru → bpy‘‘, bpy‘‘	MLCT
S_{38}	278.3	4.45	0.231	H-6→L+1 H-5→L	48 20	bpy‘, bpy‘‘ → bpy‘, bpy‘‘ bpy‘, bpy‘‘ → bpy‘, bpy‘‘	LC
S_{40}	273.1	4.54	0.597	H-6→L H-5→L+1	28 34	bpy‘, bpy‘‘ → bpy‘, bpy‘‘ bpy‘, bpy‘‘ → bpy‘, bpy‘‘	
S_{48}	248.4	4.99	0.032	H-5→L+3	71	bpy‘, bpy‘‘→ bpy‘, bpy‘‘	
S_{50}	246.6	5.03	0.052	H-6→L+3	83	bpy‘, bpy‘‘→ bpy‘, bpy‘‘	
S_{62}	235.3	5.27	0.024	H-6→L+4 H-5→L+5	11 44	bpy‘, bpy‘‘→ na’, bpy‘ bpy‘, bpy‘‘→ bpy‘, bpy‘‘	
S_{64}	233.0	5.32	0.022	H-6→L+6 H-5→L+6 H-2→L+9 H →L+11	17 14 10 10	bpy‘, bpy‘‘→ bpy‘, bpy‘‘ bpy‘, bpy‘‘→ bpy‘, bpy‘‘ Ru → bpy‘, bpy‘‘ Ru → bpy‘, bpy‘‘	

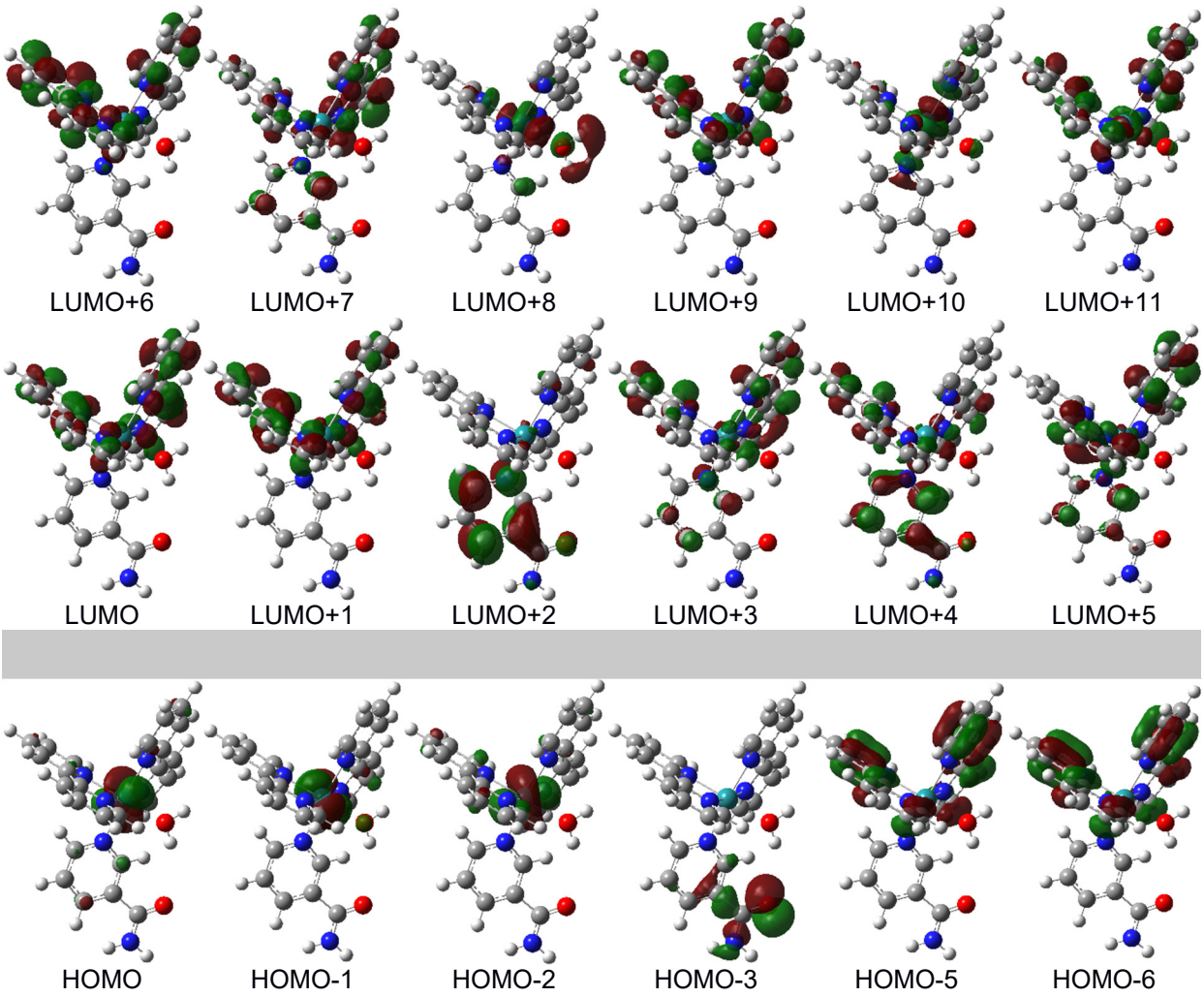

Figure 33 Molecular orbital isosurfaces of $[Ru(bpy)_2(na)(H_2O)]^{2+}$ (**2**), contributed to electronic transition with a weight of < 10%.

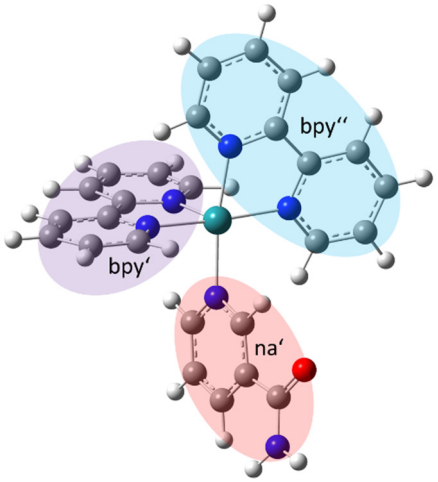

Figure 34 Structural elements of the $[Ru(bpy)_2(na)]^{2+}$ (PCI) complex.

Table 6 Calculated transitions of $[Ru(bpy)_2(na)]^{2+}$ (PCI) at the ground state geometry (TD-DFT/B3LYP/cc-PVTZ). The singlet transitions with an oscillator strength of f > 0.03 are displayed and major contributions to electronic transitions with a weight of ≥ 10%.

State	λ_{cal} [nm]	E_v [eV]	*f*	Transitions	Weight [%]	Involved ligands/metals	Transition type
S_5	427.1	2.90	0.107	H-2→L H-1→L+1	72 16	Ru → bpy', bpy'' Ru → bpy', bpy''	MLCT
S_6	407.3	3.04	0.040	H-2→L+1	71	Ru → bpy', bpy''	MLCT
S_{11}	352.8	3.51	0.071	H-2→L+2 H-1→L+2 H →L+2	10 29 32	Ru → na' Ru → na' Ru → na'	MLCT
S_{23}	315.7	3.93	0.038	H-1→L+6 H →L+7	19 65	Ru → bpy', bpy'' Ru → bpy'', bpy''	MLCT
S_{38}	278.3	4.45	0.231	H-6→L+1 H-5→L	48 20	bpy', bpy'' → bpy', bpy'' bpy', bpy'' → bpy', bpy''	LC
S_{40}	273.1	4.54	0.597	H-6→L H-5→L+1	28 34	bpy', bpy'' → bpy', bpy'' bpy', bpy'' → bpy', bpy''	
S_{48}	248.4	4.99	0.032	H-5→L+3	71	bpy', bpy''→ bpy', bpy''	
S_{50}	246.6	5.03	0.052	H-6→L+3	83	bpy', bpy''→ bpy', bpy''	
S_{62}	235.3	5.27	0.024	H-6→L+4 H-5→L+5	11 44	bpy', bpy''→ na', bpy' bpy', bpy''→ bpy', bpy''	
S_{64}	233.0	5.32	0.022	H-6→L+6 H-5→L+6 H-2→L+9 H →L+11	17 14 10 10	bpy', bpy''→ bpy', bpy'' bpy', bpy''→ bpy', bpy'' Ru → bpy', bpy'' Ru → bpy', bpy''	

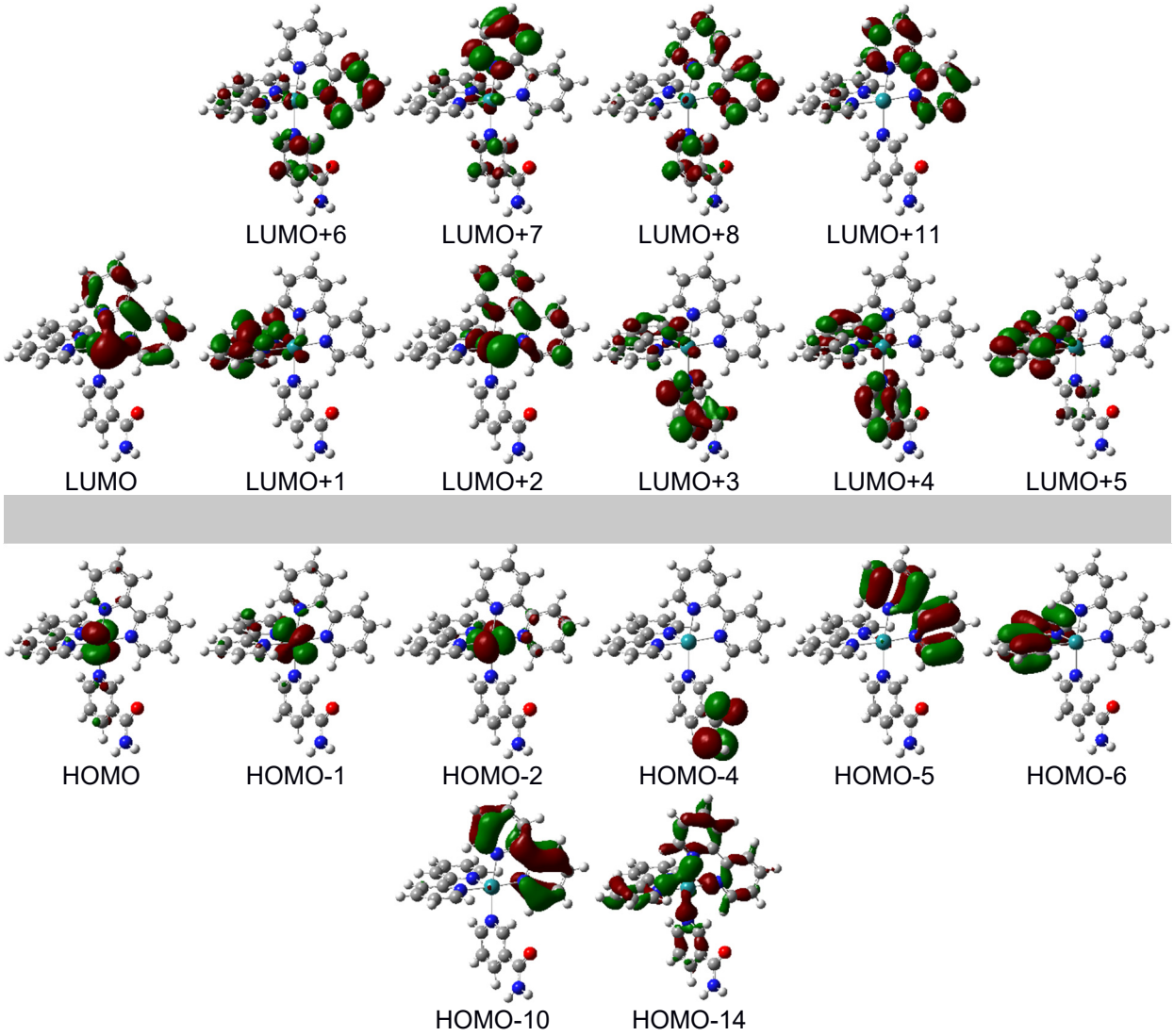

Figure 35 Molecular orbital isosurfaces of $[Ru(bpy)_2(na)]^{2+}$ (PCI), contributed to electronic transition with a weight of < 10%.

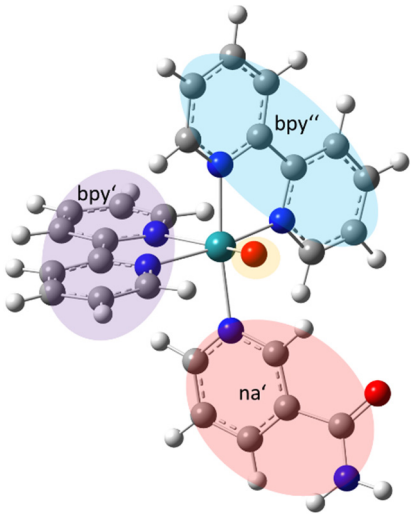

Figure 36 Structural elements of the $[Ru(bpy)_2(na)(O)]^{2+}$ (PCI=O) complex.

Table 7 Calculated transitions of $[Ru(bpy)_2(na)(O)]^{2+}$ (PCI=O) at the ground state geometry (TD-DFT/B3LYP/cc-PVTZ). The singlet transitions with an oscillator strength of f > 0.025 are displayed and major contributions to electronic transitions with a weight of ≥ 10%.

State	λ_{cal} [nm]	E_v [eV]	*f*	Transitions	Weight [%]	Involved ligands/metals	Transition type
S_4	565.5	2.19	0.027	H →L+2	95	Ru, O → bpy''	MLCT, ILCT
S_{28}	309.6	4.01	0.038	H-5→L+1 H-3→L+1	19 52	bpy', Ru → bpy' bpy', Ru, bpy'' → bpy'	MLCT, LC, ILCT
S_{33}	290.4	4.27	0.044	H-14→L H-13→L H-12→L H-4 →L+2	25 12 28 24	na', bpy', bpy'' → Ru, O PCI=O → Ru, O bpy', O, bpy'' → Ru, O bpy'' → bpy''	Mixed
S_{35}	287.8	4.31	0.069	H-11→L H-4 →L+1 H-4 →L+2	36 11 19	bpy', bpy'' → Ru, O bpy'' → bpy' bpy'' → bpy''	LMCT, ILCT, LC
S_{37}	285.4	4.34	0.140	H-11→L H-5 →L+1 H-4 →L+1	11 31 16	bpy', bpy'' → Ru, O bpy', Ru → bpy' bpy'' → bpy'	Mixed
S_{39}	281.4	4.41	0.169	H-12→L H-4 →L+2	37 17	bpy', O, bpy'' → Ru, O bpy'' → bpy''	LMCT, LC
S_{41}	278.2	4.46	0.058	H-15→L H-14→L H-13→L	26 17 22	na', bpy' → Ru, O na', bpy', bpy'' → Ru, O PCI=O → Ru, O	LMCT
S_{46}	270.5	4.58	0.039	H-15→L H-14→L	52 25	na', bpy' → Ru, O na', bpy', bpy'' → Ru, O	LMCT
S_{55}	251.7	4.93	0.060	H-5→L+4 H-3→L+4	17 68	bpy', Ru → na' bpy', Ru, bpy'' → na'	ILCT
S_{57}	249.0	4.98	0.033	H-7→L+2 H-5→L+3 H-4→L+3 H-3→L+3	20 11 36 10	na', O → bpy'' bpy', Ru → na' bpy'' → na' bpy', Ru, bpy'' → na'	ILCT
S_{59}	247.6	5.01	0.047	H-5→L+3 H-3→L+5	28 28	bpy', Ru → na' bpy', Ru, bpy'' → na'	ILCT
S_{64}	241.3	5.14	0.030	H-5→L+6 H-3→L+6 H-3→L+7	11 34 14	bpy', Ru → bpy' bpy', Ru, bpy'' → bpy' bpy', Ru, bpy'' → bpy''	LC
S_{68}	239.6	5.17	0.053	H-3→L+6 H-3→L+7	13 18	bpy', Ru, bpy'' → bpy' bpy', Ru, bpy'' → bpy''	LC, ILCT
S_{70}	237.0	5.23	0.027	H-5→L+5 H-3→L+5	42 10	bpy', Ru → na' bpy', Ru, bpy'' → na'	ILCT
S_{79}	231.1	5.37	0.025	H-4→L+6 H-4→L+8	10 18	bpy'' → bpy' bpy'' → Ru	ILCT, LMCT

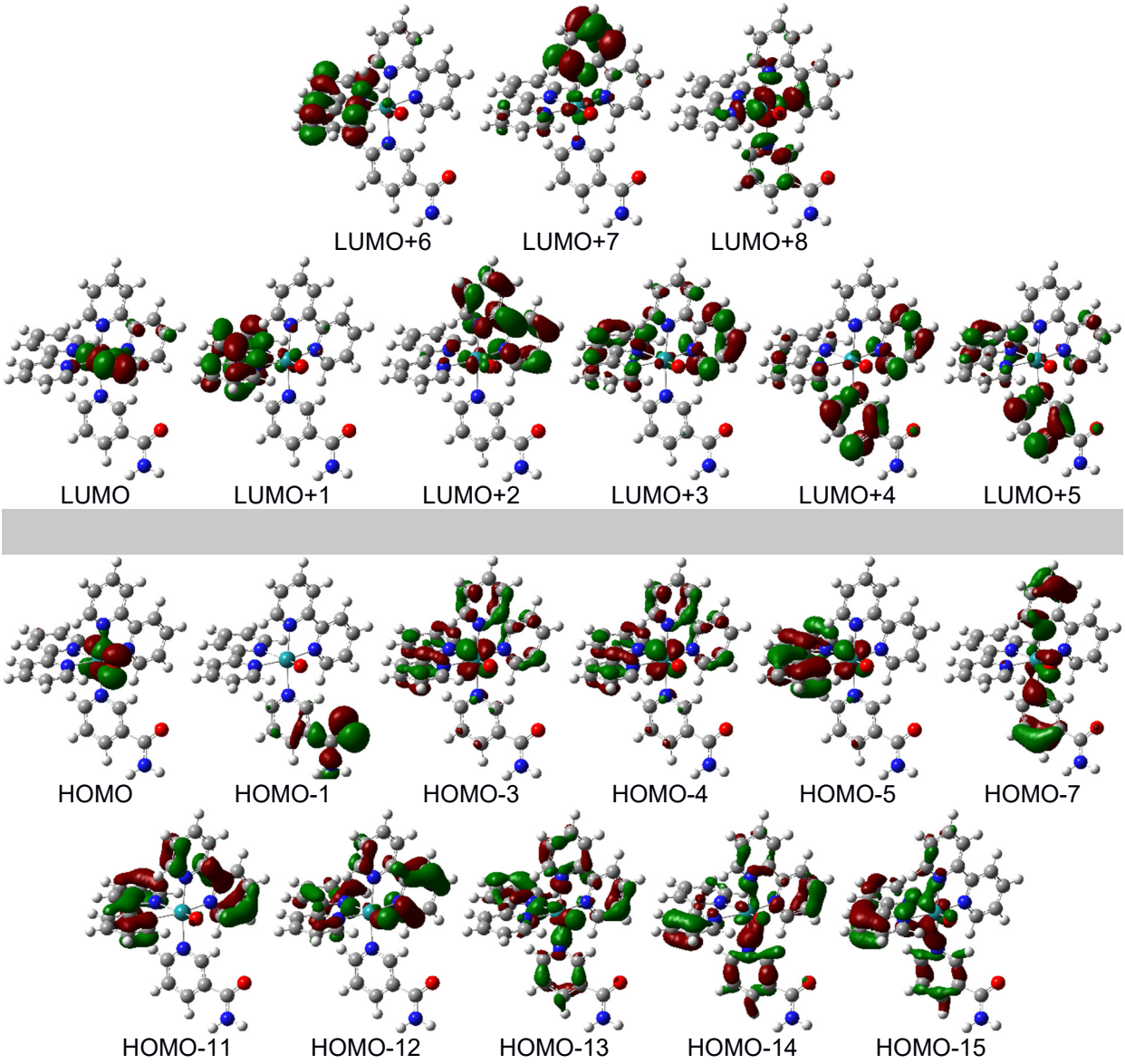

Figure 37 Molecular orbital isosurfaces of $[Ru(bpy)_2(na)(O)]^{2+}$ (PCI=O), contributed to electronic transition with a weight of < 10%.

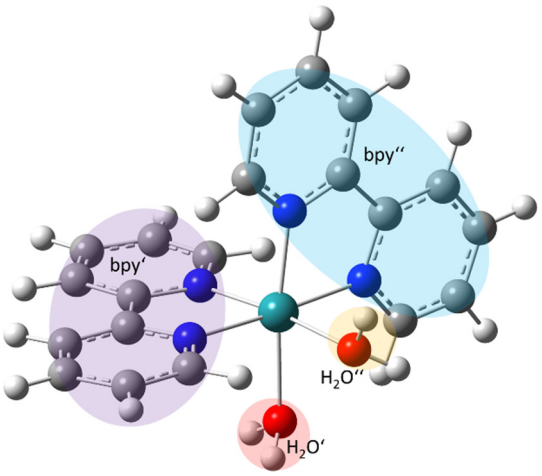

Figure 38 Structural elements of the $[Ru(bpy)_2(H_2O)_2]^{2+}$ complex.

Table 8 Calculated transitions of $[Ru(bpy)_2(H_2O)_2]^{2+}$ at the ground state geometry (TD-DFT/B3LYP/cc-PVTZ). The singlet transitions with an oscillator strength of f > 0.010 are displayed and major contributions to electronic transitions with a weight of ≥ 10%.

State	λ_{cal} [nm]	E_v [eV]	*f*	Transitions	Weight [%]	Involved ligands/metals	Transition type
S_5	425.4	2.91	0.085	H-2→L H-1→L+1 H →L+6	42 36 11	Ru → bpy', bpy'', Ru Ru → bpy', bpy'', Ru Ru → Ru	MLCT, ILCT
S_7	397.6	3.12	0.032	H →L H →L+6	14 53	Ru → bpy', bpy'', Ru Ru → Ru	MC
S_{13}	329.4	3.76	0.017	H-2→L+2	81	Ru → bpy', bpy''	MLCT
S_{19}	308.7	4.02	0.093	H-1→L+3 H →L+4 H →L+5	27 46 11	Ru → bpy', bpy'' (0.5) Ru → bpy' Ru → bpy''	MLCT
S_{21}	305.9	4.05	0.012	H-4→L+4	79	bpy', bpy'' → bpy'	LC
S_{24}	292.0	4.25	0.013	H-4→L+1 H-3→L	31 51	bpy', bpy'' → bpy', bpy'', Ru bpy', bpy'' → bpy', bpy'', Ru	LC
S_{27}	277.1	4.47	0.238	H-4→L+1 H-3→L	53 19	bpy', bpy'' → bpy', bpy'', Ru bpy', bpy'' → bpy', bpy'', Ru	LC
S_{28}	273.5	4.53	0.626	H-4→L H-3→L+1 H-2→L+4	30 39 10	bpy', bpy'' → bpy', bpy'', Ru bpy', bpy'' → bpy', bpy'', Ru Ru → bpy'	LC
S_{30}	265.0	4.68	0.014	H-2→L+7 H-1→L+7 H-1→L+9	11 34 34	Ru → H2O', H2O'', Ru Ru → H2O', H2O'', Ru Ru → Ru	MC
S_{32}	247.0	5.02	0.037	H-3→L+2	84	bpy', bpy'' → bpy', bpy''	LC
S_{33}	245.4	5.05	0.059	H-4→L+2	84	bpy', bpy'' → bpy', bpy''	LC
S_{36}	238.1	5.21	0.013	H-4→L+4 H-3→L+3 H-3→L+4	15 25 12	bpy', bpy'' → bpy' bpy', bpy'' → bpy', bpy'' (0.5) bpy', bpy'' → bpy'	ILCT
S_{41}	232.5	5.33	0.011	H-4→L+5 H-1→L+8 H →L+8	10 21 27	bpy', bpy'' → bpy'' Ru → bpy', bpy'' Ru → bpy', bpy''	MLCT
S_{42}	231.9	5.35	0.020	H-1→L+8 H →L+8	53 10	Ru → bpy', bpy'' Ru → bpy', bpy''	MLCT

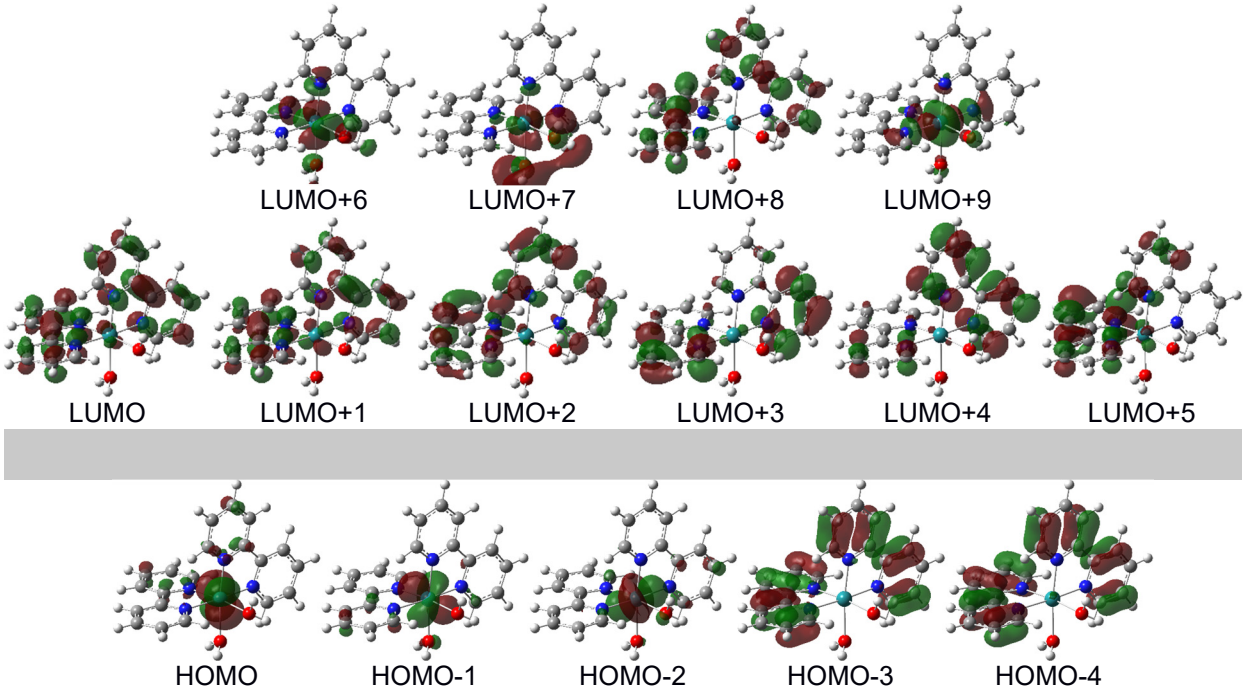

Figure 39 Molecular orbital isosurfaces of $[Ru(bpy)_2(H_2O)_2]^{2+}$, contributed to electronic transition with a weight of < 10%.

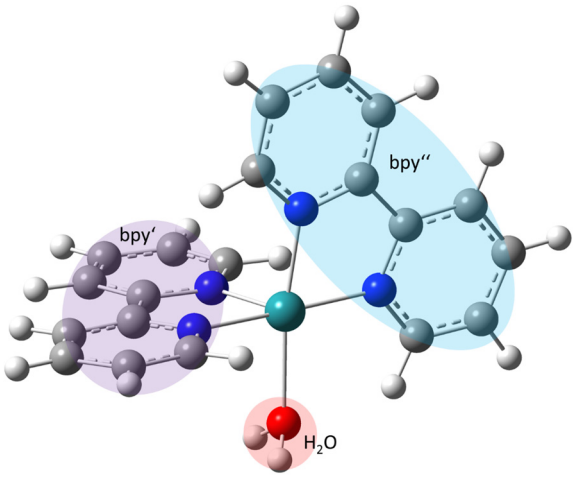

Figure 40 Structural elements of the $[Ru(bpy)_2(H_2O)]^{2+}$ complex.

Table 9 Calculated transitions of $[Ru(bpy)_2(H_2O)]^{2+}$ at the ground state geometry (TD-DFT/B3LYP/cc-PVTZ). The singlet transitions with an oscillator strength of f > 0.02 are displayed and major contributions to electronic transitions with a weight of ≥ 10%.

State	λ_{cal} [nm]	E_v [eV]	*f*	Transitions	Weight [%]	Involved ligands/metals	Transition type
S_5	399.8	3.10	0.021	H →L H →L+2	17 63	Ru → bpy'', Ru Ru → bpy'', Ru	MLCT, MC
S_7	393.0	3.15	0.040	H-2→L+1 H-1→L+1	31 38	Ru → bpy' Ru → bpy'	MLCT
S_{10}	357.0	3.47	0.037	H-2→L H-2→L+2	24 55	Ru → bpy'', Ru Ru → bpy'', Ru	MLCT, MC
S_{11}	332.1	3.73	0.032	H-3→L H →L+3	56 31	bpy'' → bpy'', Ru Ru → bpy'	LC, MLCT
S_{12}	327.5	3.79	0.023	H-3→L H →L+3	29 58	bpy'' → bpy'', Ru Ru → bpy'	LC, MLCT
S_{21}	298.2	4.16	0.041	H →L+4 H →L+5 H →L+6	14 32 21	Ru → bpy' Ru → bpy'', Ru Ru → bpy''	MLCT
S_{23}	291.6	4.25	0.037	H-2→L+4 H-1→L+5	38 25	Ru → bpy' Ru → bpy'', Ru	MLCT
S_{27}	275.4	4.50	0.105	H-4→L+1 H-2→L+5 H-1→L+6	17 19 15	bpy' → bpy' Ru → bpy'', Ru Ru → bpy''	LC, MLCT
S_{28}	273.9	4.53	0.291	H-4→L+1 H-2→L+5	39 20	bpy' → bpy' Ru → bpy'', Ru	LC, MLCT
S_{30}	261.2	4.75	0.404	H-3→L+2 H-2→L+6	46 23	bpy'' → bpy'', Ru Ru → bpy''	LC, MLCT
S_{35}	242.9	5.10	0.041	H-5→L H-4→L+3	10 53	bpy'' → bpy'', Ru bpy' → bpy'	LC
S_{41}	233.0	5.32	0.070	H-10→L H-5 →L H-3 →L+5	17 16 37	bpy', bpy'' (0.5) → bpy'', Ru bpy'' → bpy'', Ru bpy'' → bpy'', Ru	LMCT
S_{42}	232.0	5.34	0.025	H-10→L H-8 →L H-7 →L	31 23 30	bpy', bpy'' (0.5) → bpy'', Ru bpy' → bpy'', Ru bpy', bpy'' (0.5) → bpy'', Ru	ILCT
S_{43}	230.9	5.37	0.023	H-10→L H-8 →L	25 38	bpy', bpy'' (0.5) → bpy'', Ru bpy' → bpy'', Ru	LMCT

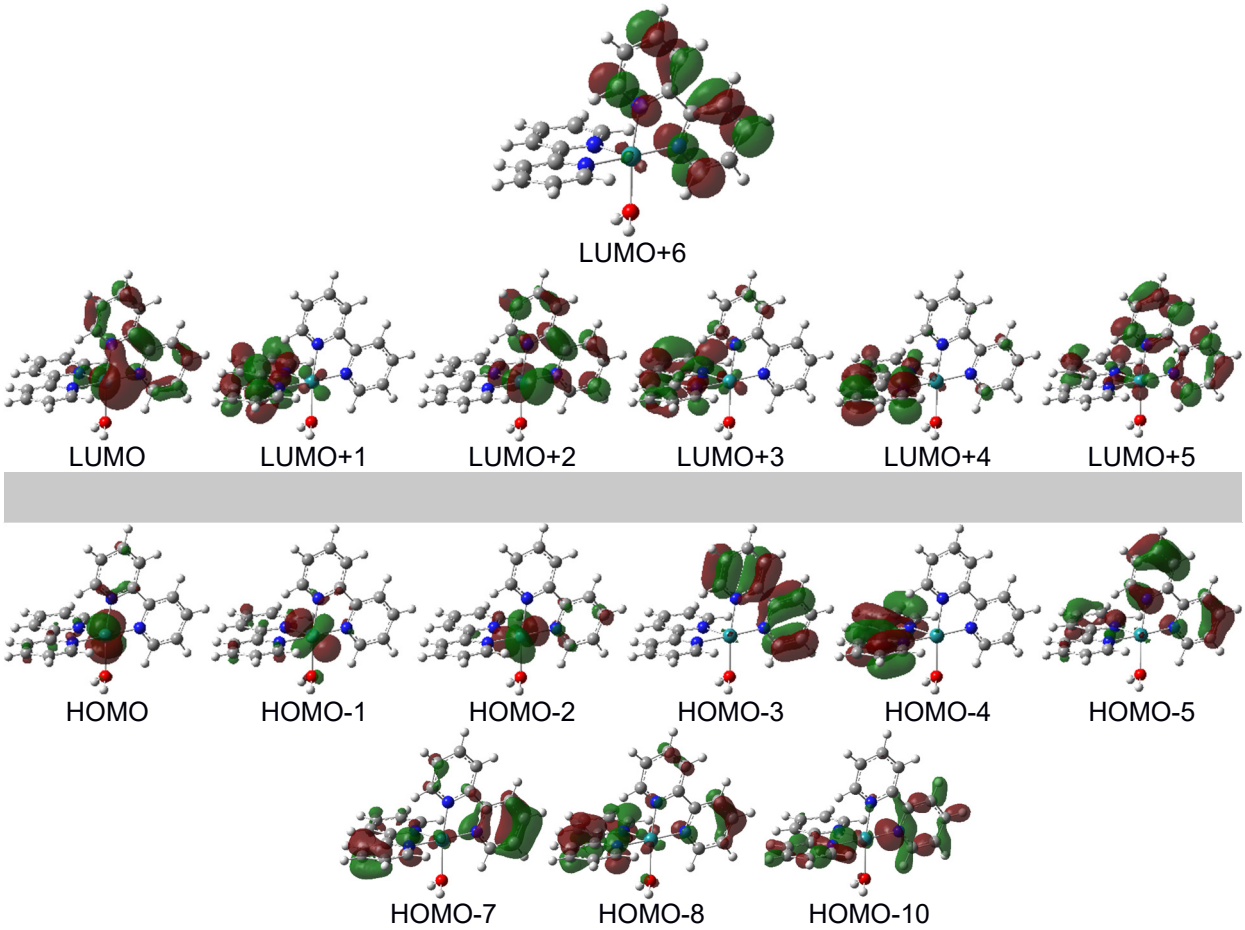

Figure 41 Molecular orbital isosurfaces of $[Ru(bpy)_2(H_2O)]^{2+}$, contributed to electronic transition with a weight of < 10%.

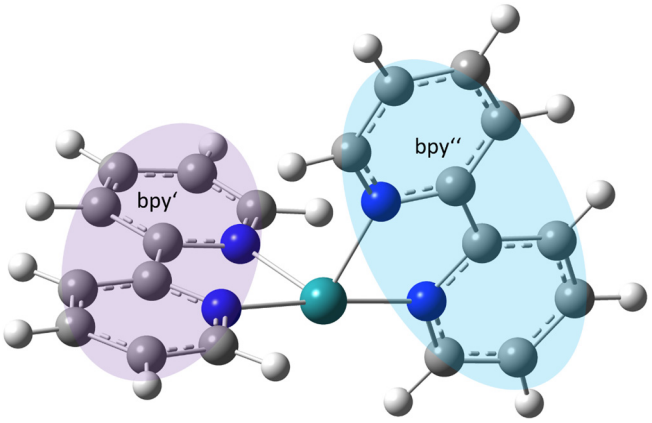

Figure 42 Structural elements of the $[Ru(bpy)_2]^{2+}$ complex.

Table 10 Calculated transitions of $[Ru(bpy)_2]^{2+}$ at the ground state geometry (TD-DFT/B3LYP/cc-PVTZ). The singlet transitions with an oscillator strength of f > 0.03 are displayed and major contributions to electronic transitions with a weight of ≥ 10%.

State	λ_{cal} [nm]	E_v [eV]	*f*	Transitions	Weight [%]	Involved ligands/metals	Transition type
S_{11}	351.2	3.53	0.087	H-2→L H-2→L+2	18 69	Ru → Ru, bpy', bpy'' Ru → Ru, bpy', bpy''	MC, MLCT
S_{15}	320.0	3.88	0.055	H-3→L+1 H →L+4	78 17	bpy', bpy'' → Ru, bpy', bpy'' Ru → bpy', bpy'' (0.5)	LMCT
S_{16}	315.6	3.93	0.039	H-4→L+1	90	bpy', bpy'' → Ru, bpy', bpy''	LMCT, LC
S_{17}	305.0	4.07	0.049	H-3→L+1 H →L+4	15 73	bpy', bpy'' → Ru, bpy', bpy'' Ru → bpy', bpy'' (0.5)	MLCT, LC
S_{24}	281.2	4.41	0.084	H-2→L+4 H-1→L+5 H-1→L+7 H →L+6	12 39 17 21	Ru → bpy', bpy'' (0.5) Ru → bpy', bpy'' (0.5) Ru → bpy', bpy'' (0.5) Ru → bpy', bpy'' (0.5)	MLCT
S_{25}	278.7	4.45	0.031	H-3→L+2 H-2→L+7 H-1→L+6 H →L+7	38 12 19 22	bpy', bpy'' → Ru, bpy', bpy'' Ru → bpy', bpy'' (0.5) Ru → bpy', bpy'' (0.5) Ru → bpy', bpy'' (0.5)	MLCT
S_{27}	273.6	4.53	0.102	H-4→L+2 H-2→L+6	53 21	bpy', bpy'' → Ru, bpy', bpy'' Ru → bpy', bpy'' (0.5)	LMCT
S_{31}	258.2	4.80	0.096	H-5→L H-4→L+3	12 57	bpy', bpy'' → Ru, bpy', bpy'' bpy', bpy'' → Ru, bpy', bpy''	LMCT
S_{32}	255.9	4.84	0.402	H-3→L+3 H-2→L+6	42 26	bpy', bpy'' → Ru, bpy', bpy'' Ru → bpy', bpy'' (0.5)	LMCT
S_{33}	252.5	4.91	0.036	H-5→L H-3→L+4	62 18	bpy', bpy'' → Ru, bpy', bpy'' bpy', bpy'' → bpy', bpy'' (0.5)	LC
S_{37}	243.2	5.10	0.050	H-10→L H-8 →L H-3 →L+4	12 15 47	bpy', bpy'' (0.5)→ Ru, bpy', bpy'' bpy', bpy'' → Ru, bpy', bpy'' bpy', bpy'' → bpy', bpy'' (0.5)	LC

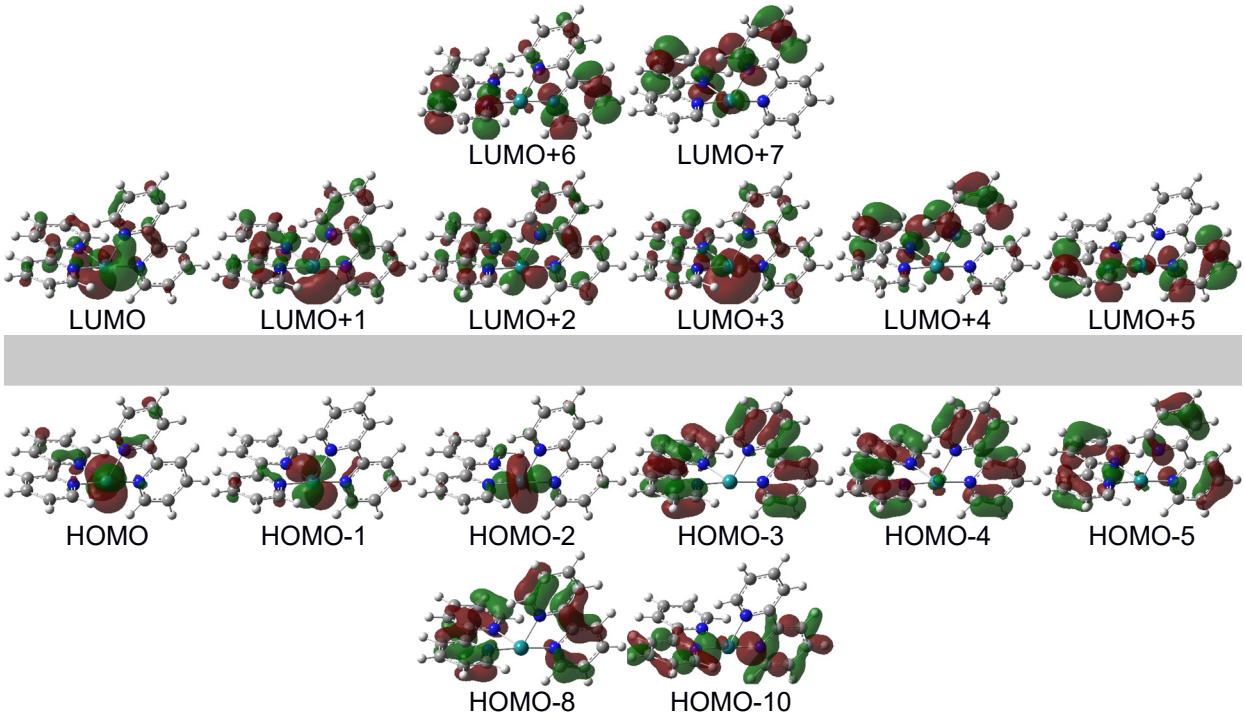

Figure 43 Molecular orbital isosurfaces of $[Ru(bpy)_2]^{2+}$, contributed to electronic transition with a weight of < 10%.

c) Geometry optimization of the ground state and selected excites states for 1 and 2

Table 11 Selected geometry optimized singlet and triplet (MC, MLCT) states of $[Ru(bpy)_2(na)_2]^{2+}$ (**1**) obtained by DFT/B3LYP/cc-PVTZ and their energy differences.

State	λ_{cal} [nm]	*f*	Transitions	Weight [%]	Involved ligands/metals	Transition type	$\Delta(T_1\text{-}X)$ [kJ/mol]	$\Delta(S_1\text{-}X)$ [kJ/mol]	$\Delta(S_5\text{-}X)$ [kJ/mol]
T_1	532.2	-	H →L H →L+1	73 16	Ru → bpy‘ Ru → bpy‘‘	MLCT (bpy)	**0**	-5.43	-6.51
T_2	512.7	-	H-2→L H →L+1	55 25	Ru → bpy‘ Ru → bpy‘‘	MLCT (bpy)	5.25	-0.18	-1.26
S_1	491.3	0.002	H →L	79	Ru → bpy‘	MLCT (bpy)	5.43	**0**	-1.08
S_2	477.2	0.002	H-1→L+1 H →L+1	11 71	Ru → bpy‘‘ Ru → bpy‘‘	MLCT (bpy)	6.44	1.00	-0.08
S_5	439.6	0.084	H-2→L H-1→L+1	59 22	Ru → bpy’ Ru → bpy‘‘	MLCT (bpy)	6.51	1.08	**0**
S_6	426.0	0.050	H-2→L H-1→L+1 H →L+1	25 45 12	Ru → bpy’ Ru → bpy‘‘ Ru → bpy‘‘	MLCT (bpy)	-	-	-
T_7	413.0	-	H →L+11	71	Ru → Ru	MC	-0.54	-5.97	-7.05
T_8	408.3	-	H-2→L+2	68	Ru → na‘	MLCT (na)	-11.89	-17.32	-18.40
S_7	391.9	0.002	H →L+2	89	Ru → na‘	MLCT (na)	12.67	7.24	6.16
S_{12}	362.0	0.041	H-2→L+2	82	Ru → na‘	MLCT (na)	-	-	-
S_{15}	346.8	0.047	H-2→L+3	71	Ru → na‘, bpy‘	MLCT (na)	-	-	-

Table 12 Geometrical properties of the optimized states of **1** from SI-Tab. 11. Given are the distances of the Ru-N bonds in Å.

Distance / [Å]	T_1	T_2	S_1	S_2	S_5	T_7	T_8	S_7
Ru-na_1	2.174	2.150	2.170	2.167	2.165	2.210	2.163	2.155
Ru-na_2	2.199	2.192	2.186	2.146	2.164	2.264	2.205	2.167
Ru-na (avg.)	**2.187**	**2.171**	**2.178**	**2.157**	**2.165**	**2.237**	**2.184**	**2.161**
Ru-N_1-bpy_1	2.120	2.129	2.121	2.103	2.098	2.100	2.137	2.103
Ru-N_2-bpy_1	2.075	2.090	2.069	2.100	2.092	2.010	2.082	2.092
Ru-N_1-bpy_2	2.015	2.074	2.075	2.097	2.106	2.082	2.060	2.101
Ru-N_2-bpy_2	2.099	2.068	2.086	2.100	2.101	2.121	2.083	2.104
Ru-N-bpy (avg.)	**2.077**	**2.090**	**2.088**	**2.100**	**2.099**	**2.078**	**2.091**	**2.100**

Table 13 Selected geometry optimized singlet and triplet (MC, MLCT) states of $[Ru(bpy)_2(na)(H_2O)]^{2+}$ (**2**) obtained by DFT/B3LYP/cc-PVTZ and their energy differences.

State	λ_{cal} [nm]	*f*	Transitions	Weight [%]	Involved ligands/metals	Transition type	$\Delta(T_1\text{-}X)$ [kJ/mol]	$\Delta(S_1\text{-}X)$ [kJ/mol]	$\Delta(S_5\text{-}X)$ [kJ/mol]
T_1	533.3	-	H →L H →L+8	45 18	Ru → bpy‘, bpy‘‘ Ru → Ru, H_2O	MC, MLCT	**0**	77.18	-77.05
T_2	519.0	-	H →L+1	82	Ru → bpy‘, bpy‘‘	MLCT	-74.90	2.28	-2.15
S_1	485.7	0.004	H →L	88	Ru → bpy‘, bpy‘‘	MLCT	-77.18	**0**	0.14
S_2	478.1	0.003	H →L+1	92	Ru → bpy‘, bpy‘‘	MLCT	-76.55	0.63	-0.49
T_5	478.6	-	H-2→L+1 H-1→L H-1→L+1 H-1→L+8 H →L	10 35 10 12 16	Ru → bpy‘, bpy‘‘ Ru → bpy‘, bpy‘‘ Ru → bpy‘, bpy‘‘ Ru → Ru, H_2O Ru → bpy‘, bpy‘‘	MLCT	30.33	107.51	-107.37
S_5	427.1	0.107	H-2→L H-1→L+1	72 16	Ru → bpy‘, bpy‘‘ Ru → bpy‘, bpy‘‘	MLCT	-77.05	0.14	**0**
T_9	426.2	-	H-2→L H-2→L+8	18 47	Ru → bpy‘, bpy‘‘ Ru → Ru, H_2O	MC, MLCT	-7.03	70.16	-70.02
S_7	394.4	0.004	H-1→L+8 H →L+3 H →L+8	13 14 35	Ru → Ru, H_2O Ru → bpy’ Ru → Ru, H_2O	MC, MLCT	-	-	-
S_9	364.3	0.015	H-1→L+2 H →L+2	29 51	Ru → na’ Ru → na’	MLCT	-86.98	-9.79	+9.93

Table 14 Geometrical properties of the optimized states of **2** from SI-Tab. 13. Given are the distances of the Ru-N and Ru-O bonds in Å.

Distance / [Å]	T_1	T_2	S_1	S_2	T_5	S_5	T_9	S_9
Ru-na	2.146	2.160	2.163	2.142	2.207	2.136	2.160	2.129
Ru-OH_2	4.095	2.267	2.201	2.186	3.260	2.210	3.639	2.265
Ru-N_1-bpy_1	2.084	2.124	2.088	2.093	2.079	2.127	2.110	2.116
Ru-N_2-bpy_1	2.097	2.092	2.078	2.090	2.086	2.085	2.115	2.094
Ru-N_1-bpy_2	2.375	2.070	2.030	2.027	2.446	2.040	2.278	2.061
Ru-N_2-bpy_2	2.151	2.056	2.104	2.084	2.167	2.077	2.107	2.100
Ru-N-bpy (avg.)	**2.177**	**2.086**	**2.075**	**2.074**	**2.195**	**2.082**	**2.153**	**2.093**

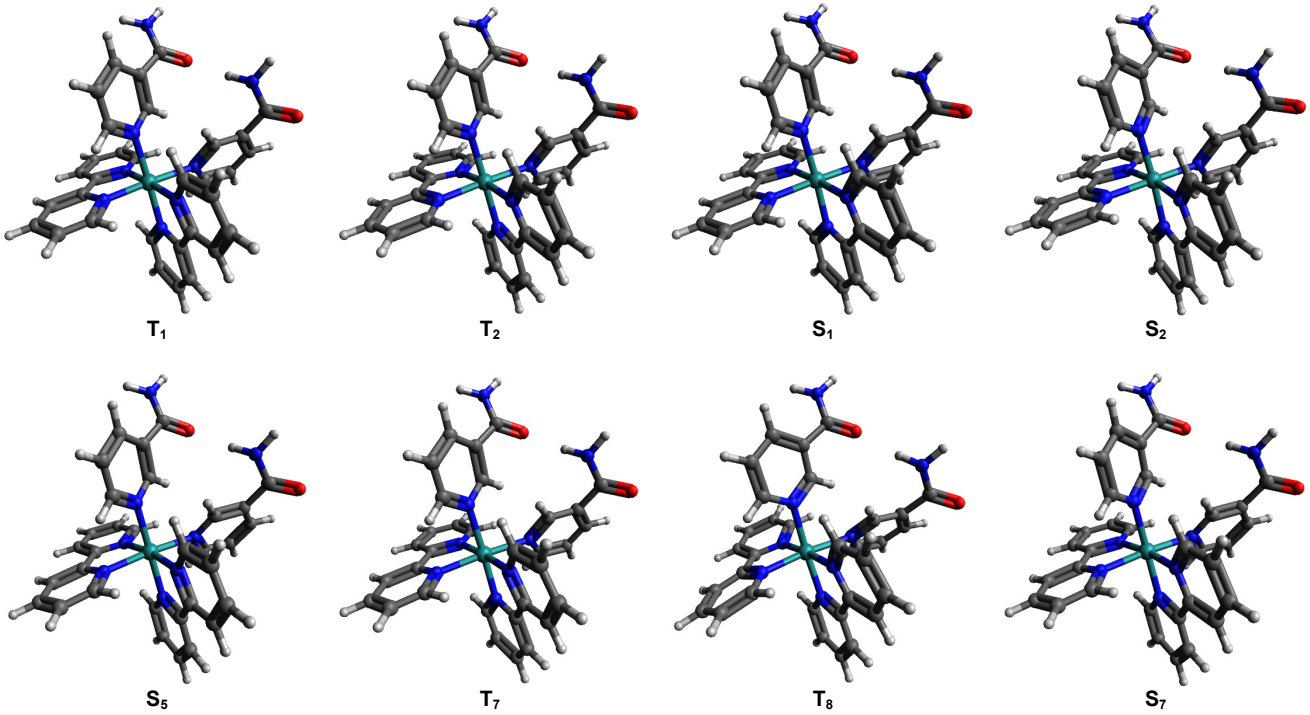

Figure 44 Structural geometries of the optimized states of **1** from SI-Tab. 11.

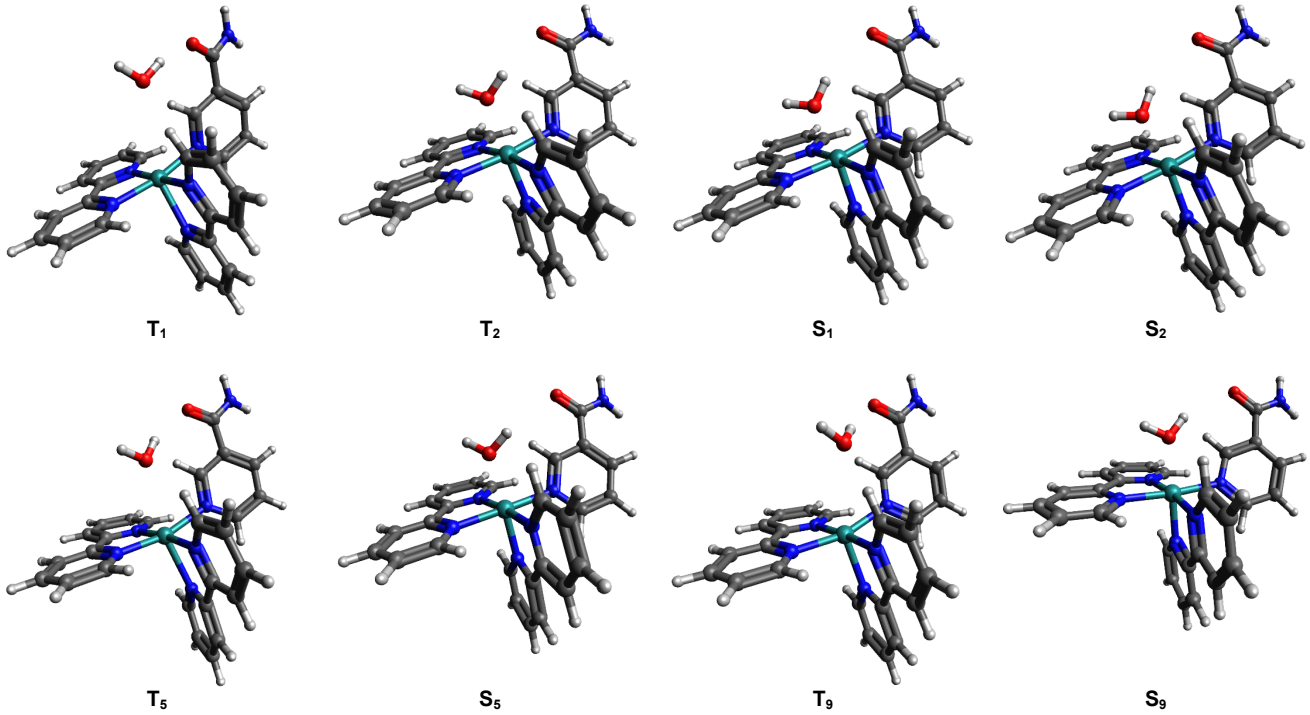

Figure 45 Structural geometries of the optimized states of **2** from SI-Tab. 13.

7. Purity of the sample $[Ru(bpy)_2(na)_2](PF_6)_2$ ($1(PF_6)_2$)

The high purity of the sample $\mathbf{1}(PF_6)_2$ was confirmed by mass spectrometry, ^{1}H-NMR and CHN-analysis. The overview mass spectrum (SI-Fig. 3) shows mainly the main peak of the complex **1** at m/z 329. 10 % of the relative intensity is observed for the species PCl (m/z 268) and $[Ru(bpy)_2(na)_2]^{2+}(PF_6)^-$ (m/z 803), where the former stems probably from a dissociation of **1** and the latter from a counterion aggregation, both occuring during the ESI process. Further observable peaks are insignificant due to their minor intensity (< 1 %).

The ^{1}H-NMR spectrum (SI-Fig. 46) is assigned in the following:

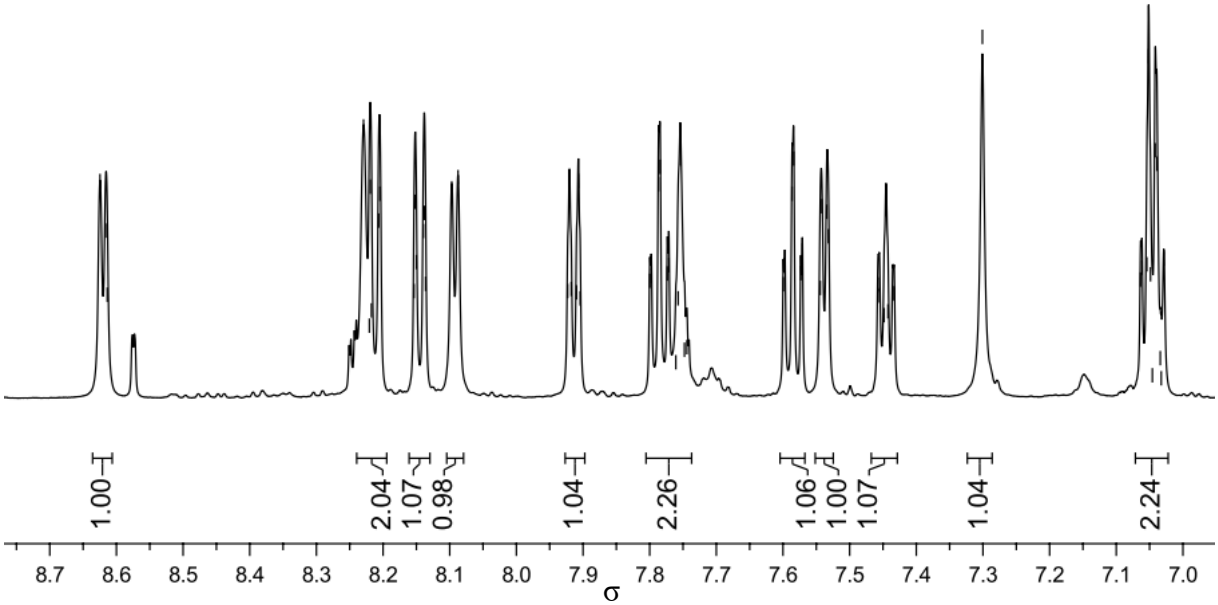

Figure 46 ^{1}H-NMR of $[Ru(bpy)_2(na)_2](PF_6)_2$ ($\mathbf{1}(PF_6)_2$) solved in acetone-d6 measured at 600.1 MHz.

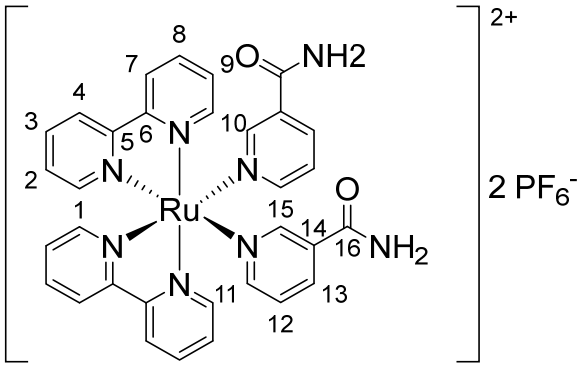

^{1}H-NMR (600.1 MHz, $(CD_3)_2CO$): δ = 8.62 (dd, $^3J_{HH}$ = 5.4 Hz, 2H, H-10), 8.23 – 8.20 (m, 4H, H-7, H-15), 8.14 (td, $^3J_{HH}$ = 8.3 Hz, $^4J_{HH}$ = 1.0 Hz 2H, H-4), 8.09 (d, $^3J_{HH}$ = 5.7 Hz, 2H, H-1), 7.91 (dt, $^3J_{HH}$ = 8.1 Hz, $^4J_{HH}$ = 1.6 Hz, 2H, H-13), 7.95 (td, $^3J_{HH}$ = 7.9 Hz, $^4J_{HH}$ = 1.4 Hz, 2H, H-8), 7.76 – 7.74 (m, 2H, unknown), 7,59 (td, $^3J_{HH}$ = 7.9 Hz, $^4J_{HH}$ = 1.5 Hz, 2H, H-3), 7.54 (dd, $^3J_{HH}$ = 5.9 Hz, $^4J_{HH}$ = 1.4 Hz, 2H, H-11), 7.45 (ddd, $^3J_{HH}$ = 7.3 Hz, $^3J_{HH}$ = 5.5 Hz, $^4J_{HH}$ = 1.3 Hz, 2H, H-9), 7.30 (s, 2H, unknown), 7.06 – 7.03 (m, , 4H, H-2, H-12) ppm.
The peaks at 7.75 and 7.30 are assigned to protons of the NH_2 group due to their singlet character.

Eventually the CHN-analysis also supports a well purity grade of the sample due to the low deviation (< 0.17%): calculated for $C_{32}H_{28}F_{12}N_8O_2P_2Ru$: C: 40.56%, H: 2.98%, N: 11.82%; found: C: 40.68%, H: 3.15%, N: 11.99%.

8. References

1. S. E. Greenough, G. M. Roberts, N. A. Smith, M. D. Horbury, R. G. McKinlay, J. M. Żurek, M. J. Paterson, P. J. Sadler and V. G. Stavros, *Physical Chemistry Chemical Physics*, 2014, **16**, 19141-19155.
2. J. M. Voss, E. M. Duffy, B. M. Marsh and E. Garand, *ChemPlusChem*, 2017, **82**, 691-694.
3. E. M. Duffy, J. M. Voss and E. Garand, *The Journal of Physical Chemistry A*, 2017, **121**, 5468-5474.
4. Y. Liu, D. B. Turner, T. N. Singh, A. M. Angeles-Boza, A. Chouai, K. R. Dunbar and C. Turro, *Journal of the American Chemical Society*, 2009, **131**, 26-27.
5. L. M. Loftus, A. Li, K. L. Fillman, P. D. Martin, J. J. Kodanko and C. Turro, *Journal of the American Chemical Society*, 2017, **139**, 18295-18306.
6. I. R. Farrell, P. Matousek, M. Towrie, A. W. Parker, D. C. Grills, M. W. George and A. Vlček, *Inorganic Chemistry*, 2002, **41**, 4318-4323.
7. I. R. Farrell, P. Matousek and A. Vlček, *Journal of the American Chemical Society*, 1999, **121**, 5296-5301.
8. S. Sato, A. Sekine, Y. Ohashi, O. Ishitani, A. M. Blanco-Rodríguez, A. Vlček, T. Unno and K. Koike, *Inorganic Chemistry*, 2007, **46**, 3531-3540.
9. A. Gabrielsson, S. Záliš, P. Matousek, M. Towrie and A. Vlček, *Inorganic Chemistry*, 2004, **43**, 7380-7388.
10. T. Lian, S. E. Bromberg, M. C. Asplund, H. Yang and C. B. Harris, *The Journal of Physical Chemistry*, 1996, **100**, 11994-12001.
11. A. A. Cordones, J. H. Lee, K. Hong, H. Cho, K. Garg, M. Boggio-Pasqua, J. J. Rack, N. Huse, R. W. Schoenlein and T. K. Kim, *Nature Communications*, 2018, **9**, 1989.
12. E. Borfecchia, C. Garino, L. Salassa, T. Ruiu, D. Gianolio, X. Zhang, K. Attenkofer, L. X. Chen, R. Gobetto, P. J. Sadler and C. Lamberti, *Dalton Transactions*, 2013, **42**, 6564-6571.
13. I. M. Dixon, S. Bonnet, F. Alary and J. Cuny, *The Journal of Physical Chemistry Letters*, 2021, **12**, 7278-7284.
14. J. D. Knoll, B. A. Albani and C. Turro, *Accounts of Chemical Research*, 2015, **48**, 2280-2287.
15. Y. Sun, Y. Liu and C. Turro, *Journal of the American Chemical Society*, 2010, **132**, 5594-5595.
16. M. K. Brennaman, J. H. Alstrum-Acevedo, C. N. Fleming, P. Jang, T. J. Meyer and J. M. Papanikolas, *Journal of the American Chemical Society*, 2002, **124**, 15094-15098.
17. E. Wachter, B. S. Howerton, E. C. Hall, S. Parkin and E. C. Glazer, *Chemical Communications*, 2014, **50**, 311-313.
18. E. Wachter and E. C. Glazer, *The Journal of Physical Chemistry A*, 2014, **118**, 10474-10486.

19. K. Garg, J. T. Engle, C. J. Ziegler and J. J. Rack, *Chemistry – A European Journal*, 2013, **19**, 11686-11695.

20. L. Salassa, C. Garino, G. Salassa, R. Gobetto and C. Nervi, *Journal of the American Chemical Society*, 2008, **130**, 9590-9597.

21. T. Mukuta, S. Tanaka, A. Inagaki, S. Koshihara and K. Onda *ChemistrySelect*, 2016, **1**, 2802-2807.

22. J. T. Hewitt, P. J. Vallett and N. H. Damrauer, *The Journal of Physical Chemistry A*, 2012, **116**, 11536-11547.

23. J. T. Hewitt, J. J. Concepcion and N. H. Damrauer, *Journal of the American Chemical Society*, 2013, **135**, 12500-12503.

24. P. S. Wagenknecht and P. C. Ford, *Coordination Chemistry Reviews*, 2011, **255**, 591-616.

25. Q. Sun, S. Mosquera-Vazquez, L. M. Lawson Daku, L. Guénée, H. A. Goodwin, E. Vauthey and A. Hauser, *Journal of the American Chemical Society*, 2013, **135**, 13660-13663.

26. Q. Sun, B. Dereka, E. Vauthey, L. M. Lawson Daku and A. Hauser, *Chemical Science*, 2017, **8**, 223-230.

27. Q. Sun, S. Mosquera-Vazquez, Y. Suffren, J. Hankache, N. Amstutz, L. M. Lawson Daku, E. Vauthey and A. Hauser, *Coordination Chemistry Reviews*, 2015, **282-283**, 87-99.

28. Y.-J. Tu, S. Mazumder, J. F. Endicott, C. Turro, J. J. Kodanko and H. B. Schlegel, *Inorganic Chemistry*, 2015, **54**, 8003-8011.

29. K. Nisbett, Y.-J. Tu, C. Turro, J. J. Kodanko and H. B. Schlegel, *Inorganic Chemistry*, 2018, **57**, 231-240.

30. A. J. Göttle, F. Alary, M. Boggio-Pasqua, I. M. Dixon, J.-L. Heully, A. Bahreman, S. H. C. Askes and S. Bonnet, *Inorganic Chemistry*, 2016, **55**, 4448-4456.

31. W. M. Wacholtz, R. A. Auerbach, R. H. Schmehl, M. Ollino and W. R. Cherry, *Inorganic Chemistry*, 1985, **24**, 1758-1760.

32. B. Durham, J. V. Caspar, J. K. Nagle and T. J. Meyer, *Journal of the American Chemical Society*, 1982, **104**, 4803-4810.

33. Gaussian 16, Revision C.01, M. J. Frisch, G. W. Trucks, H. B. Schlegel, G. E. Scuseria, M. A. Robb, J. R. Cheeseman, G. Scalmani, V. Barone, G. A. Petersson, H. Nakatsuji, X. Li, M. Caricato, A. V. Marenich, J. Bloino, B. G. Janesko, R. Gomperts, B. Mennucci, H. P. Hratchian, J. V. Ortiz, A. F. Izmaylov, J. L. Sonnenberg, D. Williams-Young, F. Ding, F. Lipparini, F. Egidi, J. Goings, B. Peng, A. Petrone, T. Henderson, D. Ranasinghe, V. G. Zakrzewski, J. Gao, N. Rega, G. Zheng, W. Liang, M. Hada, M. Ehara, K. Toyota, R. Fukuda, J. Hasegawa, M. Ishida, T. Nakajima, Y. Honda, O. Kitao, H. Nakai, T. Vreven, K. Throssell, J. A. Montgomery Jr., J. E. Peralta, F. Ogliaro, M. J. Bearpark, J. J. Heyd, E. N. Brothers, K. N. Kudin, V. N. Staroverov, T. A. Keith, R. Kobayashi, J. Normand, K. Raghavachari, A. P. Rendell, J. C. Burant, S. S. Iyengar, J. Tomasi, M. Cossi, J. M. Millam, M. Klene, C. Adamo, R. Cammi, J. W. Ochterski, R. L. Martin, K. Morokuma, O. Farkas, J. B. Foresman and D. J. Fox, Gaussian, Inc., Wallingford CT, 2016.